# Part I
# Instrument and Data Analysis

# Chapter 1

# Advances in 4D Gated Cardiac PET Imaging for Image Quality Improvement and Cardiac Motion and Contractility Estimation

**Benjamin M.W. Tsui, Tao Feng, Jizhe Wang, Jingyan Xu,**
**M. Roselle Abraham, Stefan L. Zimmerman, and Thomas H. Schindler**

**Abstract** Quantitative four-dimensional (4D) image reconstruction methods with respiratory and cardiac motion compensation are an active area of research in ECT imaging, including SPECT and PET. They are the extensions of three-dimensional (3D) statistical image reconstruction methods with iterative algorithms that incorporate accurate models of the imaging process and provide significant improvement in the quality and quantitative accuracy of the reconstructed images as compared to that obtained from conventional analytical image reconstruction methods. The new 4D image reconstruction methods incorporate additional models of the respiratory and cardiac motion of the patient to reduce image blurring due to respiratory motion and image noise of the cardiac-gated frames of the 4D cardiac-gated images. We describe respiratory motion estimation and gating method based on patient PET list-mode data. The estimated respiratory motion is applied to the respiratory gated data to reduce respiratory motion blur. The gated cardiac images derived from the list-model data are used to estimate cardiac motion. They are then used in the cardiac-gated images summing the motion-transformed cardiac-gated images for significant reduction in the gated images noise. Dual respiratory and cardiac motion compensation is achieved by combining the respiratory and cardiac motion compensation steps. The results are further significant improvements of the 4D gated cardiac PET images. The much improved gated cardiac PET image quality increases the visibility of anatomical details of the heart, which can be explored to provide more accurate estimation of the cardiac motion vector field and cardiac contractility.

**Keywords** 4D gated cardiac PET • 4D image reconstruction methods • Respiratory and cardiac motion estimation and compensation

---

B.M.W. Tsui (✉) • T. Feng • J. Wang • J. Xu • S.L. Zimmerman • T.H. Schindler
Department of Radiology, Johns Hopkins Medical Institute, Baltimore, MD, USA
e-mail: btsui1@jhmi.edu

M.R. Abraham
Department of Medicine, Johns Hopkins Medical Institute, Baltimore, MD, USA

Y. Kuge et al. (eds.), *Perspectives on Nuclear Medicine for Molecular Diagnosis and Integrated Therapy*, DOI 10.1007/978-4-431-55894-1_1

## 1.1 Introduction

The development of quantitative image reconstruction in medical imaging, including emission computed tomography (ECT) and x-ray CT [1, 2], has recently shifted from three-dimensional (3D) to four-dimensional (4D), i.e., the inclusion of the time dimension. There are two major goals for this development. First is to reduce reconstructed image artifacts due to patient motion. In particular, compensation of involuntary patient motion, e.g., respiratory motion, that causes resolution loss has received much attention [3–6]. Second is to improve the temporal resolution of dynamic images for improved detection of global and regional motion abnormalities [7, 8]. An important application is gated myocardial perfusion (MP) ECT imaging. Despite extensive research in other imaging modalities over the last two decades, MP ECT, especially gated SPECT and more recently PET, has continued to be the major biomedical imaging technique for the assessment of MP in clinical practice. The potential of extracting additional quantitative information, such as abnormalities from existing data without additional clinical studies, radiation dose or discomfort to the patients, has great significance in biomedical imaging [9–13].

The long-term goal of the study is to integrate the two aforementioned goals of the current quantitative 4D imaging reconstruction methods, i.e., to improve the quality and quantitative accuracy of the 4D cardiac gated MP PET images while reducing the blurring caused by respiratory motion (RM) and cardiac motion (CM). This is in addition to compensation of other image degrading factors, e.g., statistical noise, photon attenuation and scatter, and collimator-detector blur, to improve both spatial and temporal resolution. In this work, we present the development of a data-driven RM estimation method and quantitative 4D statistical image reconstruction methods that compensate for RM and CM separately, and for dual respiratory and cardiac (R&C) motion for improved lung and cardiac PET imaging. We hypothesize that by applying a statistical 4D image reconstruction method that accurately compensates for RM and CM and other image degrading factors, we would be able to minimize image artifacts caused by the image degrading factors, improve image resolution and reduce image noise. This would result in two significant clinical benefits, i.e., (a) reduction of false positives and false negatives for improved diagnosis, and (b) reduction of imaging time and/or radiation dose to the patient.

In addition, the much improved 4D gated cardiac PET image quality increases the visibility of details of cardiac structures. The information can be explored in a feature-based motion estimation method to determine the cardiac motion vector field and cardiac contractility.

## 1.2 Materials and Methods

### *1.2.1 Data-Driven Respiratory Motion Detection and Gating Method*

There are two general approaches to obtain respiratory gated PET data [14]. One is to use an external tracking device that directly measures a RM surrogate [3, 15]. The other is to derive RM information from the acquired data [16–19]. These data-driven RM detection methods can avoid the cost and effort and directly provide a surrogate RM signal. We developed two data-driven methods that estimated the RM from $^{13}NH_3$ and $^{18}$F-FDG cardiac gated list-mode PET data. In Fig. 1.1a, b, the $^{13}NH_3$ images show more liver uptake than the $^{18}$F-FDG images. Our data-driven method for the $^{13}NH_3$ was based on the total counts in each consecutive short segment (200–500 ms) of PET data. For the $^{18}$F-FDG, RM signal was extracted based on the axial center-of-mass of the short segment PET data. Figure 1.1c shows the relative RM gating signal amplitude as a function of time obtained from the $^{13}NH_3$ list-mode data. The estimated RM signal compared well with that obtained from an external tracking device. It was used to divide the RM into multiple respiratory gates. The respiratory gated image data were used to estimate the motion vector field of the RM and incorporated in the 4D image reconstruction method to achieve motion compensation.

From the estimated RM signal in Fig. 1.1c, we divided the list-mode data into six equal-count respiratory frames, each of which is further divided into eight cardiac-gated frames using the ECG R-wave markers. The result was a full set of dual six-frame respiratory gated and eight-frame cardiac-gated dataset. We then applied the RM compensation method described in Sect. 1.2 to the six-frame respiratory-gated dataset.

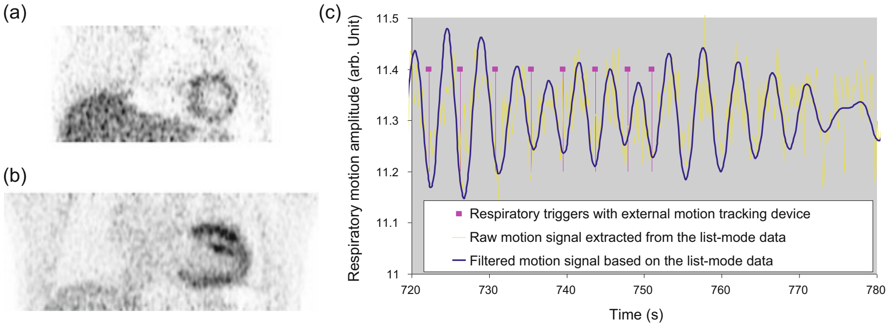

**Fig. 1.1** Sample respiratory-gated projection images from (**a**) $^{13}NH_3$ cardiac and (**b**) $^{18}$F-FDG cardiac images. (**c**) Comparison of a RM signal derived from an external tracking device and from the total count variation of the short segment projections of the $^{13}NH_3$ cardiac PET data

### *1.2.2 4D PET Image Reconstruction Methods with Attenuation, and Respiratory and Cardiac Motion Compensation*

The 4D PET image reconstruction methods used in this study were applied to the respiratory-gated and cardiac-gated projection data. Specifically, for the 4D PET image reconstruction method with dual R&C motion compensation, we divided the acquired list-mode data into six equal-count respiratory frames each with eight cardiac-gated frames as described in Sect. 1.2.1. Image reconstructions without attenuation correction were performed on this dataset to estimate the RM in lung PET studies and both RM and CM in cardiac PET studies. A special feature of our method was the modeling of the RM-induced deformations of the PET image and CT-based attenuation map in RM estimation and during PET image reconstruction for accurate and artifact-free attenuation corrected PET images.

#### 1.2.2.1 4D PET Image Reconstruction with Respiratory Motion and Attenuation Compensation

We developed a 4D PET image reconstruction method with RM and attenuation compensation to improve the image quality of $^{18}$F-FDG PET images for improved small lung lesion detection [20, 21]. First, a reference respiratory gated frame was chosen from the six equal-count respiratory frames. Then the PET image at the reference frame and the RM from the reference frame to the other respiratory-gated PET frames were estimated by minimizing the Poisson log-likelihood function. As shown in Fig. 1.2, the RM-induced deformations of both the PET image and CT-based attenuation map were modeled in the RM estimation and during PET image reconstruction. Our method is applicable to respiratory-gated PET data from current clinical PET/CT imaging procedures with only one CT-based attenuation map. We solved the image reconstruction problem in two steps: (1) estimated the RM using an iterative approach, and (2) modeled the estimated RM in a 4D OS-EM image reconstruction algorithm [21] that achieved 6 ~ 10 times acceleration over the 4D ML-EM algorithms proposed by others [22, 23]. The final estimated RM-induced deformations were applied to transform and registered all the respiratory gated frame images to the reference frame. The corresponding eight cardiac-gated frames from within the transformed respiratory-gated frames were summed resulting in the eight cardiac-gated image with respiratory compensation, that is, without RM blurring effect.

In a practical implementation of the above method [24], the RM was estimated from the 4D respiratory- gated PET images obtained without attenuation correction. The estimated RM was used in the 4D image reconstruction shown in Fig. 1.2 without further update. It provided respiratory-gated attenuation effect that matches the respiratory-gated PET images for accurate attenuation compensation.

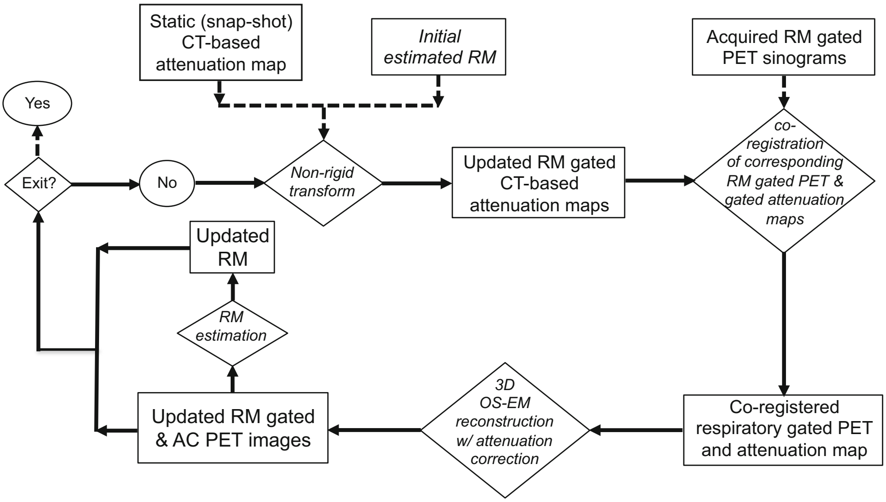

**Fig. 1.2** A flowchart of the 4D image reconstruction method with RM and attenuation compensation. A snap-shot CT image was acquired from which a static attenuation map was derived. A reference respiratory gated frame was chosen. The updated PET image at the reference frame and the RM from the reference frame to the other respiratory-gated PET frames were jointly estimated by minimizing the log-likelihood function

### 1.2.2.2 4D Image Reconstruction with Cardiac Motion Compensation

In CM compensation, a reference frame was chosen from the eight-frame cardiac-gated images. As shown in Fig. 1.3, a B-spline non-rigid transformation and registration was applied to each cardiac-gated image and registered it to the reference frame and summed. The procedure was repeated at different cardiac-gated frames in the cardiac cycle to form the CM compensated gated cardiac image set.

### 1.2.2.3 4D Image Reconstruction with Dual Respiratory and Cardiac Motion Compensation

The 4D image reconstruction with dual R&C motion compensation was achieved by combining the RM and CM compensation described in Sects. 1.2.2.1 and 1.2.2.2. After estimating the accurate RM and respiratory gated attenuation maps based on Sect. 1.2.2.1, 48-frame dual R&C gated images were obtained. For each cardiac gate, the RM compensation described in Sect. 1.2.2.1 was used. The result was RM compensated cardiac-gated images. Cardiac motion compensation was achieved by applying the same approach in Sect. 1.2.2.2. The resultant eight-frame gated cardiac images shown in Fig. 1.3 thus included both RM and CM compensation.

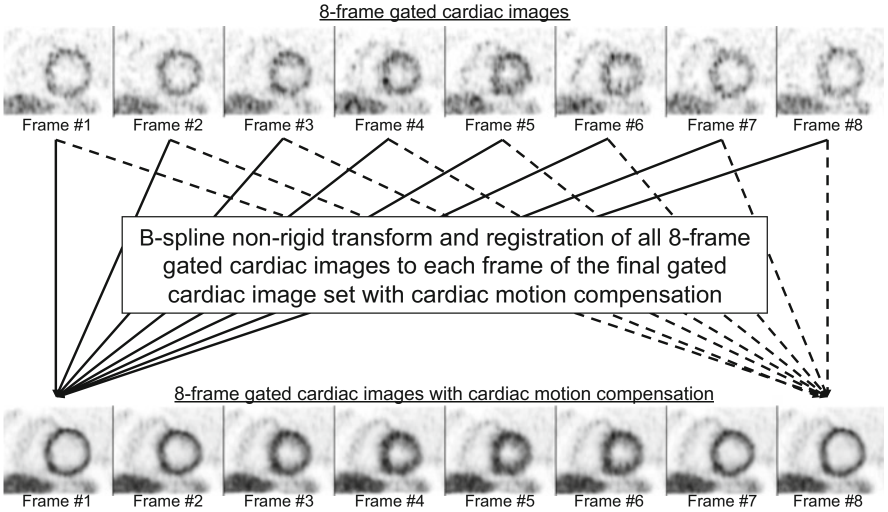

**Fig. 1.3** In the CM compensation, a B-spline non-rigid transformation and registration was applied to each cardiac-gated image and registered it to the reference frame and summed

## *1.2.3 Evaluation of the 4D PET Image Reconstruction with Respiratory and Attenuation Compensation*

We evaluated the 4D image reconstruction method with respiratory and attenuation compensation to two clinical applications. They were the detection of small lung lesions and the improvement of image quality in gated cardiac PET images. In the lung lesion detection study, we used realistic simulated 4D respiratory gated lung PET projection data. In the gated cardiac study, patient data from a $^{13}NH_3$ MP PET study and a $^{18}F$-FDG cardiac PET study were used. The goal was to assess the reduction of image resolution from blurring due to RM.

### 1.2.3.1 Evaluation Using Realistic Simulated PET Study with Small Lung Lesions

We evaluated the 4D PET image reconstruction with respiratory and attenuation compensation method using a realistic Monte Carlo (MC) simulated PET dataset from the 4D XCAT (eXtended CArdiac Torso) phantom [25]. The 4D XCAT phantom is an extension of the 4D NCAT (Nurbs-based CArdiac Torso) phantom [26], which provides realistic models of the anatomical structures of the entire human body based on the visible human data [27]. In addition, the 4D XCAT phantom includes realistic models of normal RM based on respiratory-gated CT data [28], and normal cardiac motion based on tagged MRI data. The cardiac motion model in the new 4D XCAT is based on state-of-the-art high-resolution cardiac-gated CT and tagged MRI data [29]. A 4D activity distribution phantom that modeled the uptake of the PET tracer in the different organs and a corresponding 4D attenuation coefficient distribution phantom that modeled the attenuation of different organs at the 511 keV photon energy were generated based on the 4D XCAT phantom. In addition, three small lung lesions with increased activity uptakes were inserted at different locations in the lung. The 4D activity distribution also served as the truth in the quantitative evaluation study.

Realistic respiratory-gated PET projection data were generated from the 4D activity and attenuation distributions using a combined SimSET [30] and GATE [31] MC simulation software that took advantage of the high efficiency of the former in computing the photon transport in the voxelized phantom and the ability of the latter to model the complex detector geometry and imaging characteristics of a clinical GE PET system [32]. The 4D PET image reconstruction method with RM and attenuation compensation was applied to the simulated RM-gated projection data. The results were compared to those obtained with conventional 3D and 4D image reconstruction methods without motion compensation.

#### 1.2.3.2 Evaluation Using Data from Clinical Gated Cardiac PET Studies

We also evaluated the clinical efficacy of the 4D image reconstruction method with RM and attenuation compensation using clinical $^{13}NH_3$ MP PET and $^{18}F$-FDG cardiac PET data. A GE Discovery VCT (RX) PET/CT system was used in the patient studies. Prior to the PET scan, a low-dose CT scan was acquired from the patient. In the $^{13}NH_3$ MP PET study, ~370 MBq of $^{13}NH_3$ was infused intravenously as a bolus over 10 s. List-mode PET data were acquired for 20 min. In the $^{18}F$-FDG cardiac PET study of a different patient, ~370 MBq of $^{18}F$-FDG was administered through IV injection. A list-mode PET data acquisition was performed ~60 min post injection. The 4D image reconstruction method with RM and attenuation compensation as described in Sect. 1.2.1 were applied to the acquired list-mode data. The resultant MP PET and cardiac PET images were compared to those obtained with the conventional image reconstruction method without RM compensation. Specifically, they were evaluated for improved lung lesion detection from the reduction of resolution loss due to RM blur.

### *1.2.4 Evaluation of the 4D PET Image Reconstruction Method with Dual Respiratory and Cardiac Motion Compensation*

The evaluation of the 4D PET image reconstruction method with dual R&C motion compensation was performed on the same clinical $^{13}NH_3$ MP PET and $^{18}F$-FDG cardiac PET datasets used in Sect. 1.2.3.2. Here, the goal was to assess the improvement of the quality of the gated cardiac PET images in terms of image resolution and image noise.

# 1.3 Results and Discussion

## 1.3.1 *Improvement of Small Lung Lesion Detection with Respiratory and Attenuation Compensation*

We evaluated the 4D PET image reconstruction with respiratory and attenuation compensation method using a realistic simulated PET dataset from the 4D XCAT phantom [19, 20] and the Monte Carlo (MC) method as described in Sect. 1.2.3. The method included RM detection using the data-driven gating method as described in Sect. 1.2.1. The results are shown in Fig. 1.4. The activity distribution of the 4D XCAT phantom with three small lung lesions is shown in Fig. 1.4a. The reconstructed PET images without RM compensation in Fig. 1.4b show the resolution loss due to RM blur. Also the reconstructed images with RM and attenuation compensation using the known RM from the 4D XCAT phantom (Fig. 1.4c) and using the estimated RM (Fig. 1.4d) were compared. The results indicate the effectiveness of the RM estimation method and the 4D image reconstruction

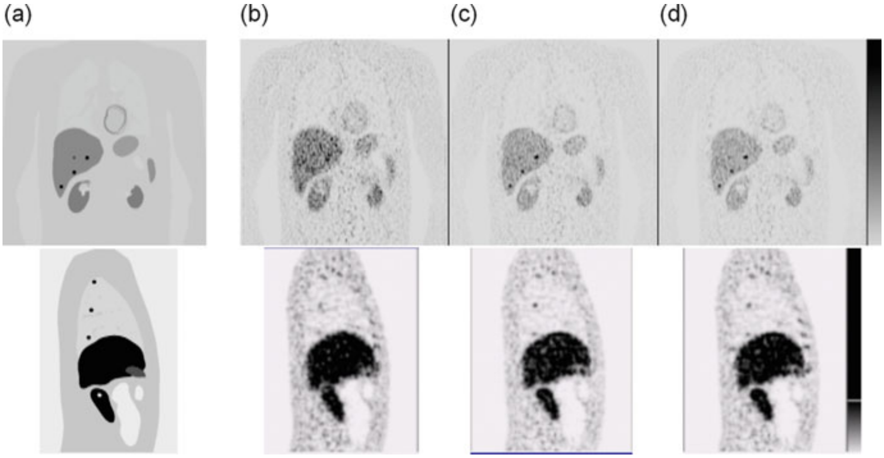

**Fig. 1.4** Results from a simulation study to evaluate the 4D PET image reconstruction with respiratory and attenuation compensation for improved lung lesion detection. A realistic MC simulated PET dataset from the 4D XCAT phantom was used. A sample (*Top row*) coronal slice and (*Bottom row*) sagittal slice through the lung showing three small lung nodules. (**a**) Activity distribution of the 4D XCAT phantom. Reconstructed images obtained from using (**b**) the 3D ML-EM method with no RM compensation, and the 4D ML-EM method (**c**) with modeling of the true RM from the 4D XCAT phantom, and (**d**) with the RM estimation described in Sect. 1.2.1

method with RM and attenuation compensation to reduce resolution loss due to RM blur and to improve small lung lesion detection in lung PET images.

### 1.3.2 Improvement of Gated Cardiac PET Images with Respiratory Motion and Attenuation Compensation

We applied the 4D image reconstruction method with RM and attenuation compensation to the clinical $^{13}NH_3$ MP PET and $^{18}$F-FDG cardiac PET datasets described in Sect. 1.2.3.2. The results are shown in Figs. 1.5 and 1.6, respectively. Figures 1.5a

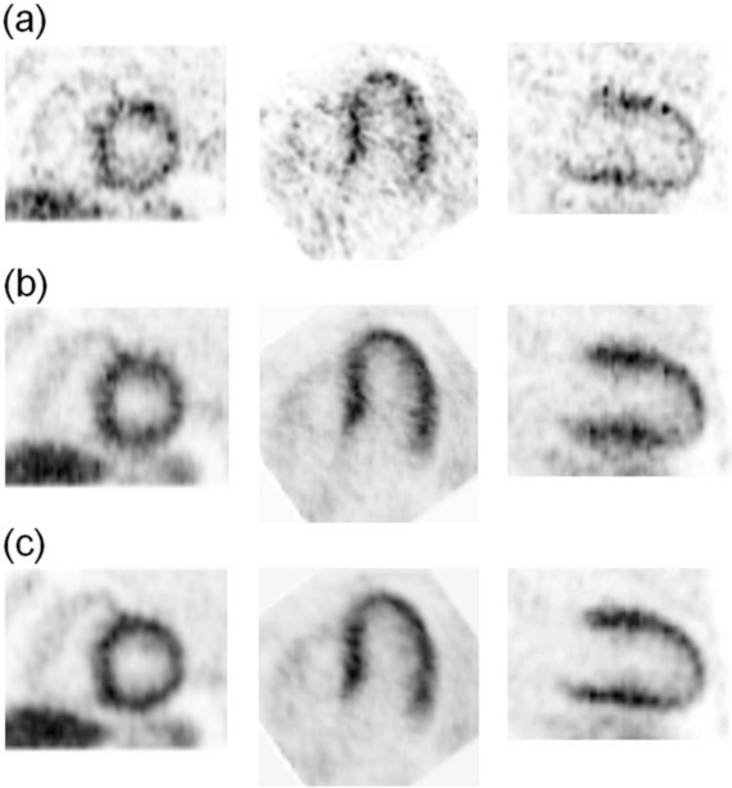

**Fig. 1.5** (**a**) Sample images from one of the six respiratory-gated frames and from selected sample (*Left*) short-axis, (*Middle*) horizontal long-axis, and (*Right*) vertical long-axis slice images obtained using a 3D OS-EM image reconstruction without any motion compensation from a $^{13}NH_3$ MP PET study. (**b**) The sum of all six respiratory gated images from (a) showing the effect of RM blur. (**c**) Corresponding sample images as in (b) obtained using the 4D OS-EM image reconstruction with RM and attenuation compensation showing the reduction of RM motion blur in the reconstructed images

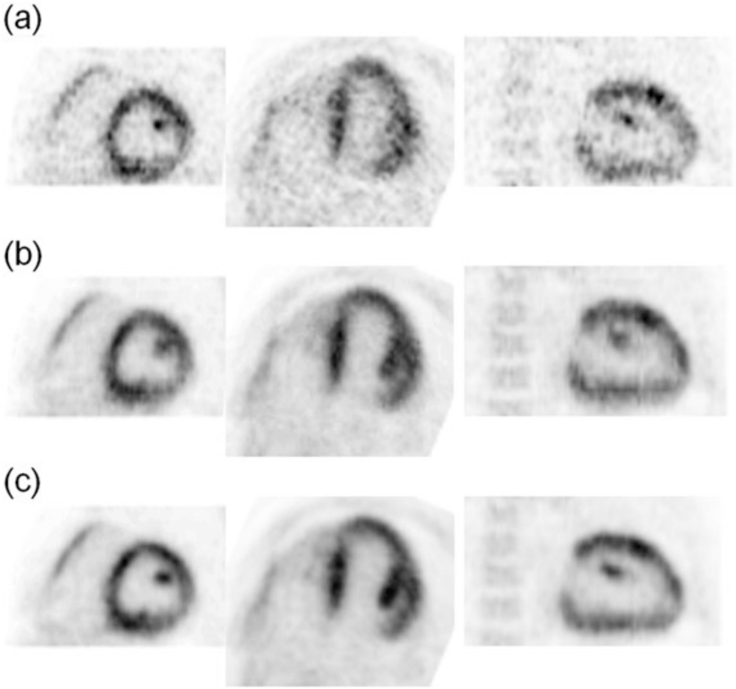

**Fig. 1.6** (**a**) Sample images from one of the six respiratory-gated frames and from selected sample (*Left*) short-axis, (*Middle*) horizontal long-axis, and (*Right*) vertical long-axis slice images obtained using a 3D OS-EM image reconstruction without any motion compensation from a $^{18}$F-FDG cardiac PET study. (**b**) The sum of all six respiratory-gated frames from (a) showing the effect of RM blur. (**c**) Corresponding sample images as in (b) obtained using the 4D OS-EM image reconstruction with RM and attenuation compensation showing the reduction of RM motion blur in the reconstructed images

and 1.6a are sample images from one of the six respiratory-gated frames and from selected sample short-axis, horizontal long-axis, and vertical long-axis slice images obtained using a 3D OS-EM image reconstruction without any motion compensation are shown. Figures 1.5b and 1.6b are the sum of all six respiratory-gated frame images demonstrating the effect of RM blur. The corresponding images obtained using the 4D OS-EM image reconstruction with RM and attenuation compensation are shown in Figs. 1.5c and 1.6c. They show the reduction of RM motion blur in the reconstructed images.

### 1.3.3 Improvement of Gated Cardiac PET Images with Dual Respiratory and Cardiac Motion Compensation

We applied the 4D image reconstruction method with dual R&C motion compensation to the clinical $^{13}NH_3$ MP PET and $^{18}$F-FDG cardiac PET datasets described in Sect. 1.2.3.2. The results are shown in Figs. 1.7 and 1.8, respectively. Figures 1.7a and 1.8a and sample images from one of the eight cardiac-gated frames and from selected sample short-axis, horizontal long-axis, and vertical long-axis slice images obtained using a 3D OS-EM image reconstruction without motion compensation. Figures 1.7b and 1.8b show the corresponding images obtained using the 4D OS-EM image reconstruction with dual R&C motion compensation. They show the significant improvement in image quality in terms of improved image resolution from RM compensation and much lower image noise level from the CM compensation.

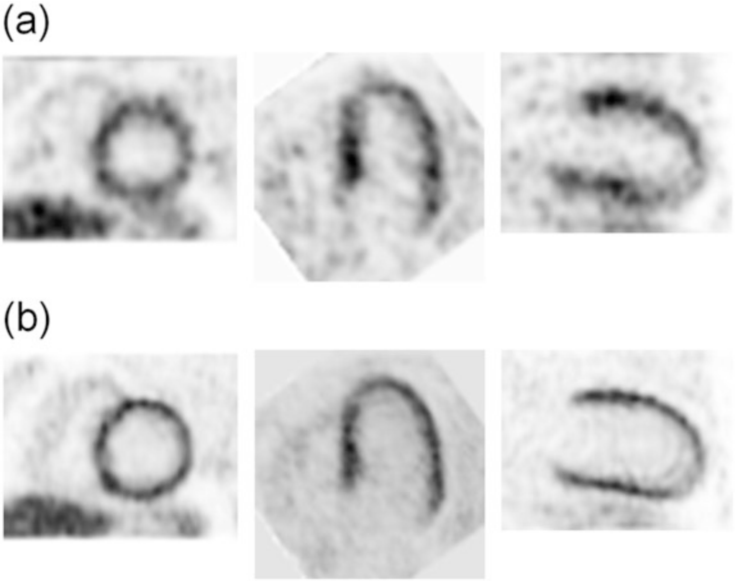

**Fig. 1.7** (**a**) Sample images from one of the eight cardiac gates from selected sample (*Left*) short-axis, (*Middle*) horizontal long-axis, and (*Right*) vertical long-axis slices images obtained using a 3D OS-EM with no motion compensation from a $^{13}NH_3$ MP PET study. (**b**) Corresponding images obtained using the 4D OS-EM with R&C motion compensation

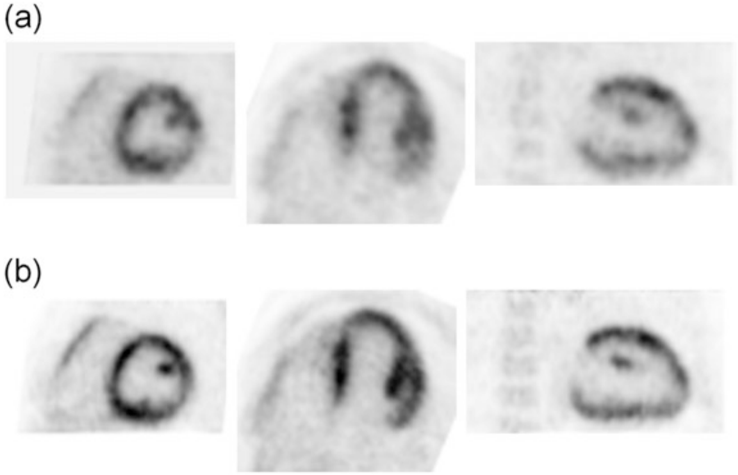

**Fig. 1.8** (**a**) Sample images from one of the eight cardiac gates from selected sample (*Left*) short-axis, (*Middle*) horizontal long-axis, and (*Right*) vertical long-axis slices images obtained using a 3D OS-EM with no motion compensation from a $^{18}$F-FDG cardiac PET study. (**b**) Corresponding images obtained using the 4D OS-EM with R&C motion compensation

## 1.4 Conclusions

Three-dimensional (3D) statistical image reconstruction methods using iterative algorithms and with models of the imaging physics and imaging system characteristics have shown to provide significant improvements in both the quality and quantitative accuracy of static SPECT and PET images. They have led to improved clinical diagnosis and, by trading off the improved image quality, for reduced patient dose and imaging time. In this work, we described newly developed 4D statistical image reconstruction methods that provided RM and CM compensation for further improvement in image quality and quantitative accuracy in PET images. We evaluated the effectiveness of the 4D image reconstruction methods using simulation and patient data.

Our results showed that a 4D image reconstruction method with RM and attenuation compensation provided quantitative lung PET images with reduced resolution loss due to RM blur and improved the detection of small lung lesions. We also evaluated a 4D image reconstruction method with dual R&C motion compensation using data from a clinical $^{13}$NH$_3$ MP PET and a clinical $^{18}$F-FDG cardiac PET study. The results showed 4D gated cardiac PET images with improved image resolution from RM compensation and much lower image noise level from the CM compensation.

The improved 4D gated cardiac PET images reveal anatomical details, such as the papillary muscle and interventricular sulcus, of the heart that were not possible with conventional 3D image reconstruction methods. The anatomical details allowed the development of feature-based myocardial motion vector estimation methods [33, 34] that overcame the aperture problem in traditional motion estimation methods. The accuracy of CM estimation will be further improved with continued improvement of the 4D image reconstruction methods and of the imaging characteristics in the next generation PET scanners that are coming into the market. It will allow extraction of new information about the contractility of the heart and provide additional diagnostic information for improved patient care.

## References

1. Nehmeh SA, Erdi YE. Respiratory motion in positron emission tomography/computed tomography: a review. Semin Nucl Med. 2008;38(3):167–76.
2. Pretorius PH, King MA, Tsui BMW, LaCroix KJ, Xia W. A mathematical model of motion of the heart for use in generating source and attenuation maps for simulating emission imaging. Med Phys. 1999;26(11):2323–32.
3. McNamara JE, Pretorius PH, Johnson K, Mukherjee JM, Dey J, Gennert MA, et al. A flexible multicamera visual-tracking system for detecting and correcting motion-induced artifacts in cardiac SPECT slices. Med Phys. 2009;36(5):1913–23.
4. Chung A, Camici P, Yang G-Z, editors. List-mode affine rebinning for respiratory motion correction in PET cardiac imaging. Medical imaging and augmented reality. Berlin/Heidelberg: Springer; 2006.
5. Chen S, Tsui BMW. Evaluation of a new 4D PET image reconstruction method with respiratory motion compensation in a CHO study. J Nucl Med 2011: 150.
6. Chen S, Tsui BMW. Evaluation of a 4D PET image reconstruction method with respiratory motion compensation in a patient study. Society of nuclear medicine annual meeting. San Antonio; 2011: J Nucl Med. 2011. p. 2023.
7. Lee T-S, Higuchi T, Lautamäki R, Bengel F, Tsui BMW. Task-based evaluation of a 4D MAP-RBI-EM image reconstruction method for gated myocardial perfusion SPECT using a human observer study. Phys Med Biol. 2015;60:6789–809.
8. Lee T-S, Tsui BMW. Optimization of a 4D space-time gibbs prior in a 4D MAP-RBI-EMReconstruction method for application to gated myocardial perfusion SPECT. Proceeding of the fully three-dimensional image reconstruction meeting in radiology and nuclear medicine. 2009. p. 122.
9. Tang J, Lee T-S, He X, Segars WP, Tsui BM. Comparison of 3D OS-EM and 4D MAP-RBI-EM reconstruction algorithms for cardiac motion abnormality classification using a motion observer. IEEE Trans Nucl Sci. 2010;57(5):2571–7.
10. Tang J, Segars WP, Lee T-S, He X, Rahmim A, Tsui BMW. Quantitative study of cardiac motion estimation and abnormality classification in emission computed tomography. Med Eng Phys. 2011;33:563–72.
11. Gilland DR, Mair BA, Bowsher JE, Jaszczak RJ. Simultaneous reconstruction and motion estimation for gated cardiac ECT. IEEE Trans Nucl Sci. 2002;49(5):2344–9.
12. Mair BA, Gilland DR, Sun J. Estimation of images and nonrigid deformations in gated emission CT. IEEE Trans Med Imaging. 2006;25(9):1130–44.

13. Lee T-S, Tsui BMW. Evaluation of corrective reconstruction method for reduced acquisition time and various anatomies of perfusion defect using channelized hotelling observer for myocardial perfusion SPECT. IEEE nuclear science symposium and medical imaging conference record. 2010. p. 3523–6.
14. Dawood M, Buther F, Lang N, Schober O, Schafers K. Respiratory gating in positron emission tomography: a quantitative comparison of different gating schemes. Med Phys. 2007;34: 3067–6.
15. Klein GJ, Reutter BW, Ho MH, Reed JH, Huesman RH. Real-time system for respiratory-cardiac gating in positron tomography. IEEE Trans Nucl Sci. 1998;45:2139–43.
16. Chung A, Camici P, Yang G-Z. List-mode affine rebinning for respiratory motion correction in PET cardiac imaging. In: Medical imaging and augmented reality. Berlin: Springer; 2006. p. 293–300.
17. Büther F, Stegger L, Wübbeling F, Schäfers M, Schober O, Schäfers KP. List mode-driven cardiac and respiratory gating in PET. J Nucl Med. 2009;50:674–81.
18. Klein GL, Reutter BW, Huesman RH. Data-driven respiratory gating in list mode cardiac PET. J Nucl Med. 1999;40:113p.
19. Lamare F, Ledesma Carbayo MJ, Cresson T, Kontaxakis G, Santos A, Cheze Le Rest C, Reader AJ, Visvikis D. List-mode-based reconstruction for respiratory motion correction in PET using non-rigid body transformations. Phys Med Biol. 2007;52:[68].
20. Chen ST, Tsui BMW. Accuracy analysis of image registration based respiratory motion compensation in respiratory-gated FDG oncologcial PET reconstruction. In: IEEE nuclear science symposium & medical imaging conference. Dresden; 2008. p. M06-417.
21. Chen S, Tsui BMW. Four-dmiensional OS-EM PET image reconstruction method with motion compensation. In: Fully three-dimensional image reconstruction in radiology and nuclear medicine. Beijing; 2009. p. 373–6.
22. Li TF, Thorndyke B, Schreibmann E, Yang Y, Xing L. Model-based image reconstruction for four-dimensional PET. Med Phys. 2006;33:1288–98.
23. Qiao F, Pan T, Clark JW, Mawlawi OR. A motion-incorporated reconstruction method for gated PET studies. Phys Med Biol. 2006;51:3769–83.
24. Chen S, Tsui BMW. Joint estimation of respiratory motion and PET image in 4D PET reconstruction with modeling attenuation map deformation induced by respiratory motion. J Nucl Med. 2010;51(supplement 2):523.
25. Segars WP, Sturgeon G, Mendonca S, Grimes J, Tsui BMW. 4D XCAT phantom for multimodality imaging research. Med Phys. 2010;37(9):4902–15.
26. Segars WP. Development of a new dynamic NURBS-based cardiac-torso (NCAT) phantom, PhD dissertation, The University of North Carolina, May 2001.
27. Segars WP, Tsui BMW. MCAT to XCAT: the evolution of 4-D computerized phantoms for imaging research. Proc IEEE. 2009;97(12):1954–68.
28. Segars WP, Mori S, Chen G, Tsui BMW. Modeling respiratory motion variations in the 4D NCAT Phantom. In: IEEE medical imaging conference. 2007. p. M26-356.
29. Segars WP, Lalush D, Frey EC, Manocha D, King MA, Tsui BMW. Improved dynamic cardiac phantom based on 4D NURBS and tagged MRI. IEEE Trans Nucl Sci. 2009;56:2728–38.
30. Lewellen TK, Harrison RL, Vannoy S. The simset program. In: Monte Carlo calculations in nuclear medicine, Medical science series. Bristol: Institute of Physics Publication; 1998. p. 77–92.
31. Jan S, et al. GATE: a simulation toolkit for PET and SPECT. Phys Med Biol. 2004; 49(19):4543.
32. Shilov M, Frey EC, Segars WP, Xu J, Tsui BMW. Improved Monte-Carlo simulations for dynamic PET. J Nucl Med Suppl. 2006;47:197.
33. Wang J, Fung GSK, Feng T, Tsui BMW. A papillary muscle guided motion estimation method for gated cardiac imaging. In: Nishikawa RM, Whiting BR, Hoeschen C, editors. Medical imaging 2013: physics of medical imaging, Proc. of SPIE, vol. 8668. Washington: SPIE; 2013. p. 86682G.
34. Wang J, Fung GSK, Feng T, Tsui BMW. An interventricular sulcus guided cardiac motion estimation method. Conference record of the 2013 I.E. nuclear science symposium and medical imaging conference, Seoul, 2013;October 27–November 2. p. 978–84.

# Chapter 2
# The Need for Quantitative SPECT in Clinical Brain Examinations

**Hidehiro Iida, Tsutomu Zeniya, Miho Yamauchi, Kazuhiro Koshino, Takashi Temma, Satoshi Iguchi, Makoto Yamazaki, Junichiro Enmi, Naoya Kondo, Nobutoku Motomura, and Jyoji Nakagawara**

**Abstract** This report describes details of the requirements and practical procedures for quantitative assessments of biological functional parametric images of the brain using $^{123}$I-labeled tracers and clinical SPECT systems. With due understanding of the physics and the biological background, this is considered achievable even under clinical environments, provided that data are appropriately acquired, processed, and analyzed. This article discusses how potential hurdles have been overcome for quantitatively assessing quantitative functional parametric images in clinical settings, with successful examples that provided additional clinically useful information.

**Keywords** SPECT • Quantitation • $^{123}$I-labeled radiopharmaceuticals • Reconstruction • Functional imaging

## 2.1 Introduction

Current clinical practice using SPECT relies largely on the interpretation of qualitative images reflecting physiologic functions. However, a quantitative analysis could provide further information to assist in the interpretation of disease status and treatment decisions. Methodological progress has made a quantitative determination of physiological functions through imaging feasible for brain scans, including parameters like the cerebral blood flow (CBF) and cerebral flow reactivity (CFR) after pharmacological vasodilatation and also neuro-receptor functions and others.

---

H. Iida (✉) • T. Zeniya • M. Yamauchi • K. Koshino • T. Temma • S. Iguchi • M. Yamazaki •
J. Enmi • N. Kondo
Department of Investigative Radiology, National Cerebral and Cardiovascular Center
Research Institute, 5-7-1, Fujishiro-dai, Suita City, Osaka 565-8565, Japan
e-mail: iida@ri.ncvc.go.jp

N. Motomura
Toshiba Medical Systems Corporation, 1385 Shimoishigami, Toshigi, Otawara City, Japan

J. Nakagawara
Department of Neurosurgery, Comprehensive Stroke Imaging Center, National Cerebral and
Cardiovascular Center, 5-7-1, Fujishiro-dai, Suita City, Osaka 565-8565, Japan

Y. Kuge et al. (eds.), *Perspectives on Nuclear Medicine for Molecular Diagnosis and Integrated Therapy*, DOI 10.1007/978-4-431-55894-1_2

The usefulness of such data has generally been limited to research due to the logistical complexity of quantitative examinations. Extensive work has then been carried out to make quantitative study doable in clinical environments, and some relevant study protocols are today generally accepted in clinical institutions in Japan.

Statistics show that 20 % of all SPECT clinical scans, namely approximately 20,000 scans annually, are carried out for the brain, mostly on patients with neurological (67 %) and cerebral vascular diseases (33 %), which is a much larger number than in other countries. Quantitative assessments of CBF (mostly with CFR) using $^{123}$I-iodoamphetamine (IMP) comprise 5.6 % of all SPECT scans. Further, software programs assisting in the diagnosis are utilized with most brain scans, employing statistical analysis such as the 3D-SSP of Minoshima and others [1–5].

$^{123}$I-IMP and other $^{123}$I-labeled tracers such as $^{123}$I-iomazenil and $^{123}$I-FP-CIT are approved for clinical use and can be employed in a quantitative analysis for demonstrating biological parametric images. Attenuation correction and scatter correction are necessary factors when conducting quantitative studies. Additional unique error of septal penetration is present when employing $^{123}$I-labeled radiopharmaceuticals.

With SPECT scans there is the advantage over PET in the availability of the necessary scanner in clinical institutions. Availability of radiopharmaceuticals is another factor which would make conducting of such clinical research simple and straightforward. Standardization of the techniques is essential to be able to generate quantitative functional images that are consistent among institutions and SPECT scanners. This is important particularly when applying diagnosis-assisting software programs, to ensure consistent results independent of the SPECT devices installed at different institutions. The ability to refer to and compare results from different institutions or databases created at different institutions also requires that quantitative and reproducible results are needed.

This article describes how an integrated system was developed to enable a quantitative assessment of images of biological functions consistent among institutions in clinical setting with $^{123}$I-labeled radiopharmaceuticals. To achieve this we describe the physics and technical background needed for the quantitation. Application and verification of the developed software packages as clinical diagnostic tools, and how users have been supported, will also be discussed for $^{123}$I-IMP, $^{123}$I-IMZ, and $^{123}$I-FP-CIT examinations.

## 2.2 Requirements for Quantitative Reconstructions in SPECT

### *2.2.1 Scatter Correction*

It is commonly accepted that the scatter and attenuation occurring in an object are the two major error factors with SPECT, and these need to be compensated for in the quantitative imaging. One technique to estimate the scatter distribution is to acquire projection data for additional energy windows in addition to the main window that covers the main peak. Selecting two additional windows below and above the main peak, the so-called triple-energy window (TEW) [6] method, is a commonly applied technique, in which acquired counts of the lower and upper windows are subtracted from those of the main window, and the reconstruction is then performed using the scatter-subtracted projection data. An advantage of this technique is that the procedures automatically compensate for the photons penetrating the collimator (see below).

An alternative approach is based on estimating the scatter from the scatter-uncorrected reconstructed images using the attenuation coefficient distribution. A formulation like the Klein-Nishina formula is commonly applied to simulate the scatter projection for a given tracer distribution and is termed the single scatter simulation (SSS) method [7]. This calculation can also be performed by Monte Carlo simulation (MCS), where simplification is effective to accelerate the calculations and ensure minimal loss of accuracy [8]. One further simplified approach is also feasible, by referring to the emission and attenuation data available in the projection domain; this was originally proposed by Meikle et al. [9] and was further optimized for $^{99m}$Tc [10], $^{201}$Tl [11, 12], and $^{123}$I [13] in our group. A scatter fraction is empirically defined for a radioisotope as a function of the attenuation factor, which is then used to scale the simulated scatter distribution. This is the transmission-dependent convolution subtraction (TDCS) method and is applied to the geometric mean projection data. A number of verification studies have been carried out to ensure the accuracy of this method, but it must be noted that accuracy with the SSS and MCS theoretical methods is often limited because a number of factors are not taken into account. Our earlier work by a careful Monte Carlo simulation demonstrated that a non-negligible amount of scatter originates from outside objects such as the detector and scanner itself [14] and that this may be a source of errors if not taken into account.

With the software developed by our group for quantitative SPECT reconstruction (QSPECT), we have incorporated MCS- and TDCS-based scatter correction methods, and extensive work has shown support for this in the verification of the TDCS method for brain SPECT examinations. Due to the robustness and applicability when combined with other correction procedures, all results in the following will be with the TDCS scatter correction.

### 2.2.2 Septal Penetration in the Collimator

In addition to scatter and attenuation, $^{123}$I has a further error arising from penetrating photons generated by high-energy gamma rays (>500 keV) emitted from the $^{123}$I. These penetrating photons cause a down-scatter through the collimator and escaping photons from the scintillator, resulting in non-negligible levels of bias in

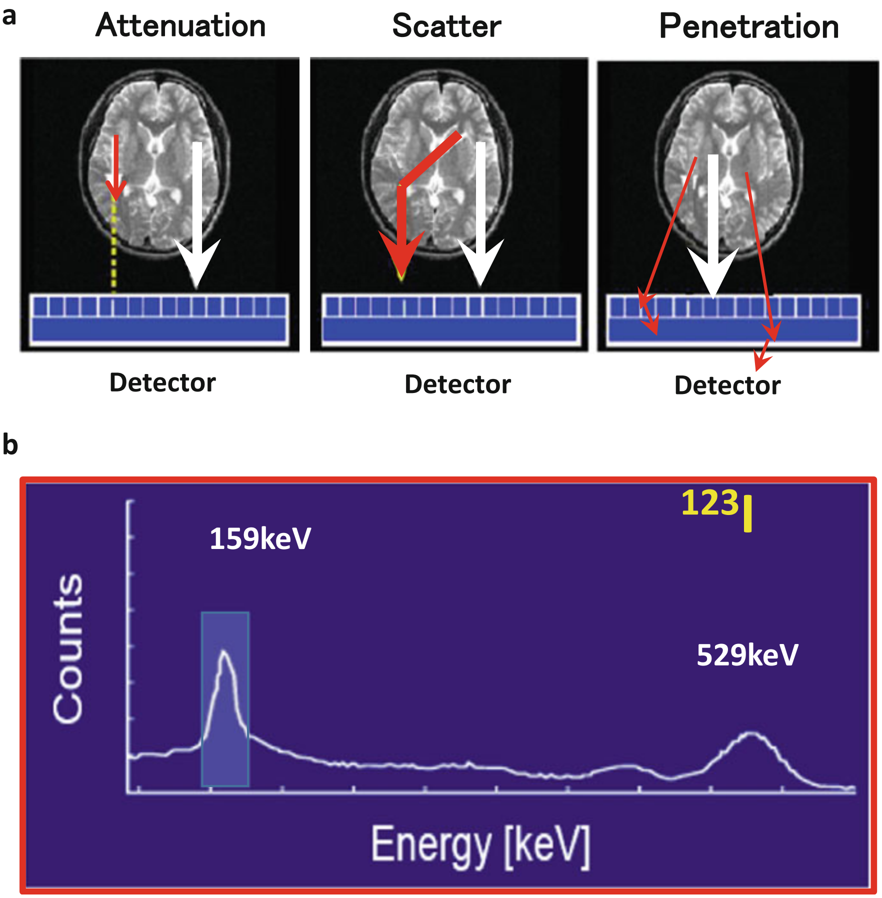

**Fig. 2.1** (**a**) Error sources which need to be compensated for in quantitative reconstruction of brain SPECT images, attenuation, scatter, and photon penetration. (**b**) Energy spectrum for $^{123}$I in a typical LEHR collimator. The significantly high background signal is a source of errors, caused by the high-energy photons emitted by the $^{123}$I itself

the energy spectrum and therefore an offset in the projection data for the selected energy window (see Fig. 2.1).

Here it must be noted that the magnitude of the offset in the projection data due to the penetrating photons varies dependent on the collimator. With typical low-energy collimator sets, this represents a large amount, due to the thin walls of such collimators, while with typical $^{123}$I-specifically designed collimator, the amount of offset is suppressed, due to thicker collimator walls. An example of a comparison of projection data obtained from two collimator sets of a typical low-energy high-resolution collimator (LEHR-para) and a $^{123}$I-specific low-medium-energy general-purpose collimator (LMEGP-para) from one vendor is shown in Fig. 2.2. Collimator penetration is clearly visible with LEHR-para, but

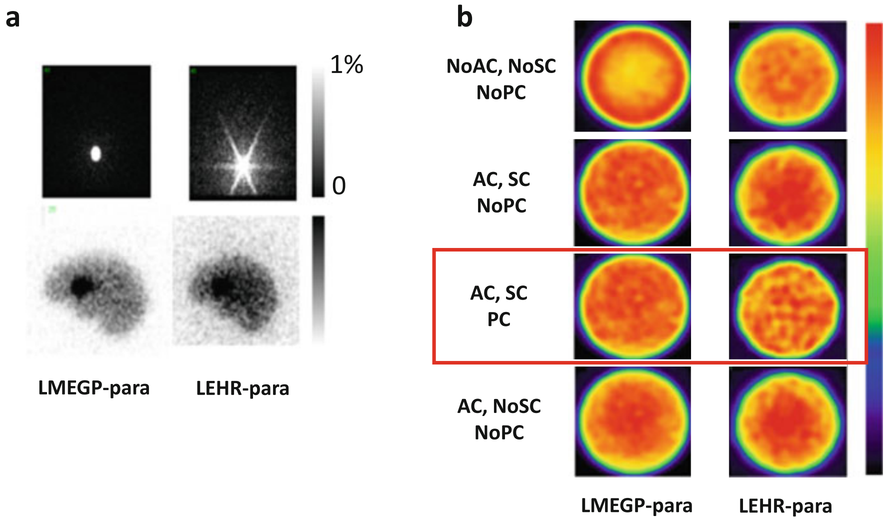

**Fig. 2.2** (**a**) Typical projection data for a syringe-shaped phantom (*left*) and for a striatum phantom from Radiology Support Devices (Long Beach, LA, USA) (*right*) measured with $^{123}$I-dedicated LMEGP-para and conventional LEHR-para collimator sets. (**b**) Reconstructed images for a uniform cylindrical phantom filled with $^{123}$I-solution with and without attenuation correction (AC), scatter correction (SC), and photon penetration correction (PC). Different amounts of photon penetration are clearly visible as a high background outside the phantom on the projection data. In the projection data of the striatum phantom, striatum-to-whole brain ratio is also altered due to the penetrating photons. The reconstructed images also became different when not compensated. An appropriate correction procedure is important to compensate for the penetration for each set of the collimator

not with LMEGP-para for a $^{123}$I-syringe and also on the striatal brain phantom (Fig. 2.2a). This difference causes the different reconstructed images of uniform cylindrical phantoms (Fig. 2.2b). It is important to note that the counts are decreased in the center of the cylindrical phantom when the attenuation correction is not applied to the data obtained with LMEGP-para collimator, while the decreased counts in the center is not visible with LEHR-para. The TEW technique is effective to compensate for the penetrating high-energy photons. With the scatter correction performed by the TEW technique, these penetrating photons are automatically compensated for. This is practical and effective, but at the expense of increased statistical noise.

In the QSPECT software, the penetration component is determined empirically for a collimator, as an extension of the TDCS scatter correction, as described in an earlier report [13].

### 2.2.3 Attenuation Correction

The Chang method [15] is the most common approach for attenuation correction (AC) in brain SPECT. This method utilizes an attenuation coefficient (μ) map which is commonly generated by detecting the head contours of the reconstructed images to which the AC is applied. The μ map can also be obtained from CT or from images of other modalities. The AC factors are then estimated for each pixel as an average over the 360° views with the attenuation coefficient (μ) map and is multiplied into the non-AC reconstructed images. The Chang method is empirical but the results are considered acceptable in most brain examinations. For the quantitative reconstruction, a uniform μ map is feasible if errors $< 5\ \%$ are accepted in the deep parts of the brain. However, absolute values have to be carefully defined so as to make the pixel counts of the reconstructed images independent of the size of the object. This is also the case if a CT-based μ map is utilized in the reconstruction.

### *2.2.4 Attenuation Coefficient Map*

Two possibilities are given to define the attenuation μ map in QSPECT software. One is to import externally generated attenuation μ maps, typically calculated from the Hounsfield unit (HU) images generated from a CT scan. Careful attention is needed to correct for the beam hardening effects when converting the attenuation map assessed with the continuous and rather low-energy photons to the quantitative HU and μ values corresponding to photons with single energy included in the energy window. Another possibility is to generate a homogeneous μ map by detecting the head contours. Extensive efforts have been made to provide the best accuracy in the head-contour detection algorithm, and a threshold was determined from the sinogram rather than the projection or the reconstructed images, and sine wave constraint was applied to the scatter-uncorrected data when defining the edge of the sinogram. Reconstruction was made for the filtered sinogram, and a threshold was applied again to determine the head contour, ensuring that an accurate head contour is generated. An empirically defined attenuation coefficient which effectively included the contribution of the bone value was then applied [13].

An attenuation coefficient map is utilized for the attenuation correction during the OSEM procedures and also for the scatter and penetration correction prior to the reconstruction if one utilizes one of the SSS, MCS, or TDCS methods for scatter correction. This attenuation coefficient map was utilized during the OSEM procedures as well as for the scatter and penetration correction prior to the reconstruction, by using the TDCS method as discussed earlier.

### *2.2.5 Implementation of the Collimator Aperture Model*

It has been shown that implementation of a collimator aperture during the forward projection process on the three-dimensional domain makes the SPECT reconstruction more accurate [16]. Effects of this are increased, resulting in improved contrast and also suppression of statistical noise. The collimator aperture model shown in

Fig. 2.4 was implemented with the QSPECT reconstruction software for both the geometric mean and normal projection data. See further below.

### *2.2.6 SPECT Reconstruction*

Two methods are known to quantitatively reconstruct images in the brain SPECT which will be discussed here. The filtered back projection (FBP) method is the one and has been the standard for reconstruction. For the FBP, the scatter correction has to be applied to the projection data before the reconstruction, and TEW is a well-established technique compensating for the septal penetration during the reconstruction. An attenuation correction is performed after the reconstruction in most cases based on the Chang method with an edge detection technique to generate homogeneous μ maps. The use of CT-based attenuation coefficient images is also possible, but selection of the absolute μ values needs careful consideration, and there are no published reports on how consistent results can be obtained with this technique with different equipment arrangements. A preliminary study carried out in Europe [17] showed unacceptable levels of variation and inconsistencies among sites. The reasons for the inconsistencies are unknown, but it was suggested that further careful evaluations are needed to standardize the detailed procedures. Although the FBP approach is straightforward and has been considered a standard, the method is limited when implementing new functionality to maximize the accuracy and image quality.

An alternative reconstruction method for SPECT is based on the maximum-likelihood expectation maximization (MLEM) algorithm, in which images are calculated with iterative procedures. Attenuation can be implemented in the forward projection process, so that the calculated reconstructed images are corrected for attenuation. The *o*rdered-*s*ubset maximum-likelihood *e*xpectation *m*aximization (OSEM) method is often utilized to accelerate convergence, as will be discussed later in this article. It must be noted that the TEW-based scatter correction includes correction also for the penetration, while currently the existing simulation-based scatter correction method does not include a penetration correction, and thus requires further development.

The QSPECT software employs the OSEM approach. A schematic representation of the process of the reconstruction in QSPECT software is shown in Fig. 2.3. Systematic errors arise due to neglecting higher μ values in the skull, but the effect is within ±5 % in the middle part of the brain and also in other areas outside the cerebral tissue [13]. The following three formulations were implemented in the program. Suitable formulation can then be selected to best fit each clinical protocol.

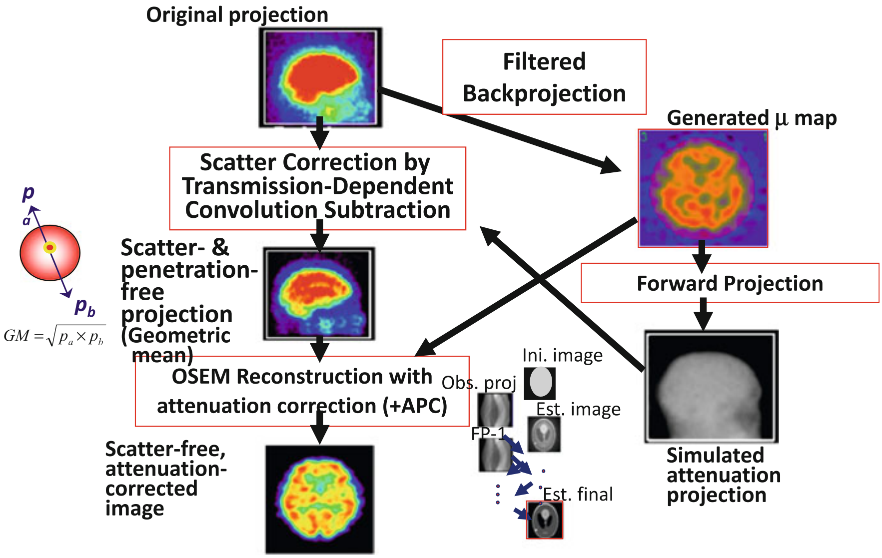

**Fig. 2.3** Diagram illustrating the quantitative reconstruction protocol implemented in the QSPECT reconstruction software. The emission data are initially reconstructed with filtered back projection (top right image) to allow the brain outline to be determined and the μ map for the attenuation correction to be determined by assigning a uniform attenuation coefficient value of 0.1603 $\text{cm}^{-1}$ to the detected brain volume. The μ map is forward projected to provide the attenuation projections for the scatter correction to calculate scatter- and penetration-compensated projection. The scatter correction is carried out using TDCS method; thus, the projection data becomes geometric mean data. Then, OSEM reconstruction is applied with the attenuation correction to generate the attenuation and scatter corrected images. The collimator aperture correction (APC) can also be applied in the reconstruction process using Eq. (2.2) (Figure is from Iida et al. [28])

#### 2.2.6.1 OSEM on 2D Domains for the Pre-scatter Corrected Geometric Mean Projection

The first formulation is essentially identical to the one also described in earlier studies [9–11, 13]. Reconstruction is performed for each two-dimensional tomographic slice, with the projection corrected for scatter before the reconstruction. The pixel counts of the reconstructed image $\lambda_j^{n+1}$ are calculated from the counts of the previous image $\lambda_j^{n}$. The scatter compensated projection data by the TDCS method [18] was applied, and the formulation for the geometric mean projection data is given as follows:

$$\lambda_j^{n+1} = \frac{\lambda_j^n}{\sum\limits_{i \in S_n} c_{ij}} \sum_{i \in S_n} \frac{c_{ij} y_i}{\left( \sum\limits_k c_{ik} \lambda_k^n \right) \exp(-\mu L_i)} \tag{2.1}$$

where $y_i$ is the count in the projection data corrected for the scatter and the collimator penetration, $c_{ij}$ is a factor for the contributions from the projection pixel to the image pixel, $\exp(-\mu L_i)$ is the net attenuation factor for each of the geometric mean projections. Note that the projection data has to be corrected before the reconstruction calculations, eg by the TDCS scatter correction.

#### 2.2.6.2 OSEM on 3D Domains for the Pre-scatter Corrected Geometric Mean Projection

This formulation includes the collimator aperture correction, and the reconstruction is carried out nearly wholly in a three-dimensional domain. The scatter compensated projection data by the TDCS method [18] was applied, giving the formulation for the geometric mean projection data as follows:

$$\lambda_j^{n+1} = \frac{\lambda_j^n}{\sum\limits_{i \in S_n} c_{ij} w_{ij}} \sum_{i \in S_n} \frac{c_{ij} w_{ij} y_i}{\left( \sum\limits_k c_{ik} w_{ik} \lambda_k^n \right) \exp(-\mu L_i)} \tag{2.2}$$

where $w_{ij}$ represents the collimator dependent blurring of the spatial resolution shown in Fig. 2.4. Note that the projection data has to be corrected for the scatter before the reconstruction calculations as in the eq. 2.1 in which $y_i$ is the geometric mean projection data already corrected for scatter by means of the TDCS method, and $c_{ij}$ represents the calculation of the geometric mean.

#### 2.2.6.3 OSEM on 3D Domains Including the Scatter Correction Process

This formulation includes the scatter correction process during the reconstruction as follows:

$$\lambda_j^{n+1} = \frac{\lambda_j^n}{\sum\limits_i c_{ij} w_{ij}} \sum_{i \in S_n} \frac{c_{ij} w_{ij} y_i}{\left\{ \sum\limits_k c_{ik} w_{ik} \lambda_k^n \exp\left( -\sum\limits_m \mu_{ikm} l_{ikm} \right) \right\} + s_i} \tag{2.3}$$

The scatter projection at the i-th iteration, $s_i$, has to be estimated at each iteration either by the SSS or MCS methods from the i-th reconstructed images. It is also possible to use the TEW-based scattered projection for $s_i$. In QSPECT, an

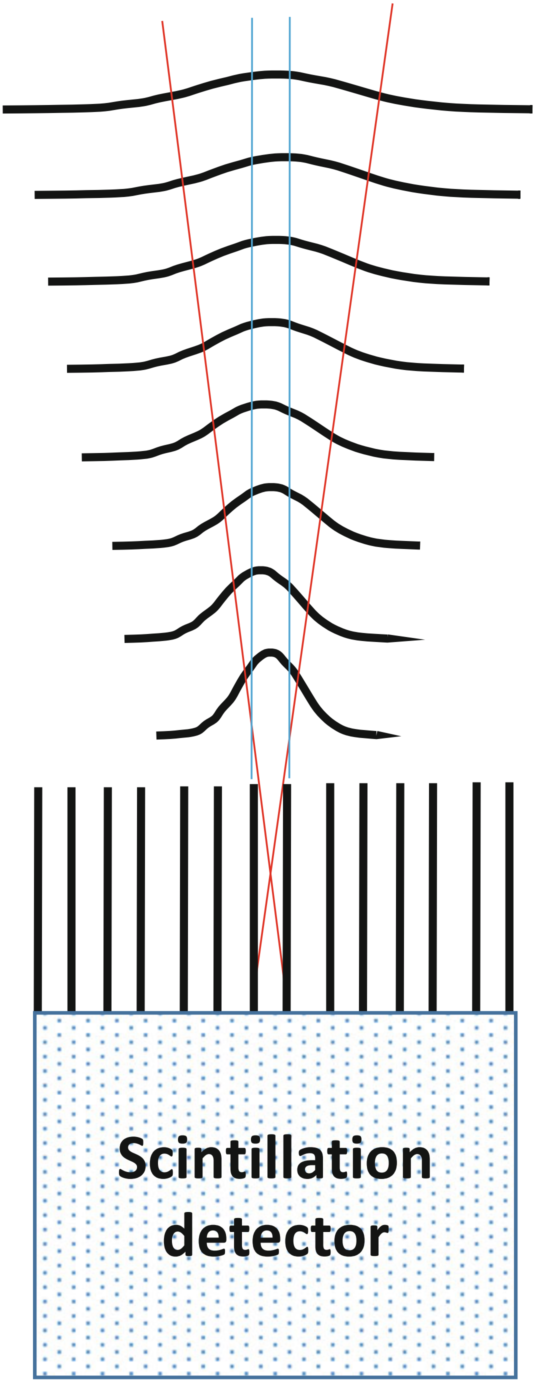

**Fig. 2.4** The model for collimator aperture correction implemented in the QSPECT reconstruction software. Spatial resolution was assumed to decrease linearly with the distance from the collimator with an initial value. The contribution weights, $w_{ij}$, calculated from this model were implemented in Eqs. (2.2) and (2.3), which compensated for the blurring effects due to the collimator aperture

accelerated MCS [8] is implemented. Consequently, $y_i$ it is not necessarily the geometric mean but may be the normal projection.

### *2.2.7 Calibration to Bq/mL*

The QSPECT program is designed so that the pixel values correspond to the radioactivity concentration, the cps/mL. An experiment with a syringe filled with a $^{123}$I-labeled radioactive pharmaceutical of known radioactivity gives a calibration factor to convert the pixel counts to the absolute radioactivity concentration which has units of Bq/mL. The accuracy of the absolute quantitation was ± 10 % for $^{123}$I in uniform cylindrical phantoms provided that the diameter is less than 16 cm. For the future, this feature could be of use in internal dosimetry quantitation of radiotherapy agents such as $^{177}$Lu peptides.

### *2.2.8 Dead Time Count Loss*

The counting rate performance should be sufficiently high in clinical SPECT scanners, e.g., count losses $<1$ % up to a counting rate of 70 kcps. This would hold for $^{99m}$Tc and other commonly used SPECT radiopharmaceuticals, but may not in $^{123}$I-labeled tracers. The true counting rate of the system could be much higher than the observed rate for the given main window, attributed to the incidence of a large amount of penetrating photons originated from the high-energy gamma rays ($>$500 keV). Particularly, low-energy dedicated collimators such as LEHR collimators can accept large amounts of penetrating photons, and there may be a significant counting loss at counting rates much below 70kcps. Errors could be mostly in phantom experiments but may be smaller in clinical scans. It is however important to confirm the maximum counting rate that maintains the linearity of the SPECT counts to the true radioactivity.

## 2.3 Phantom Experiments

A number of studies have been carried out to evaluate the adequacy of the QSPECT reconstruction programs. The experiments were on geometrically shaped phantoms such as cylindrical phantoms and also on phantoms simulating the cerebral blood flow distribution and striatum structure with realistic head contours and skull structures. These phantom experiments are useful in validating the reconstruction procedures and also to ensure quality control of the data acquisition procedures.

### 2.3.1 Uniform Cylindrical Phantom

The cylindrical phantom gives information of how uniform images are obtained for uniform distributions of radioactivity. Image homogeneity could be degraded by several factors in relation to inappropriate corrections for attenuation, to scatter and penetration, and also to the insufficient quality control. The quality control includes the procedures for adjusting and correcting for inhomogeneous sensitivity, mistuned position linearity, misaligned center of rotation, large attenuations in the head holder, and other factors. Experiments to confirm the homogeneity for uniform phantom are highly suggested to ensure that the regional activity quantitation is not suffered from one of error factors mentioned above. However, it should be noted that inappropriate definition of the head contour and inconsistently defined attenuation coefficient values in relation to the presence of the skull may not be evaluated from the uniform cylinder phantom experiment.

### 2.3.2 3D Brain Iida Phantom for CBF Quantitation

Geometrically shaped phantoms are limited in simulating realistic head contours, the presence of the bone and trachea, and also the realistic radioactivity distribution. Therefore, dedicated brain-simulating phantoms are often desired to evaluate the overall accuracy of reconstructed images in realistic situations. We have developed a three-dimensional brain phantom (Iida phantom) that simulates the CBF distribution in cortical gray matter, with bone, trachea, and realistic head contours [19]. As shown in Fig. 2.5, accuracy of the QSPECT software can be evaluated by referring regional radioactivity concentration on the reconstructed images with those of design images of this phantom. This experiment would be useful if one wish to evaluate the accuracy of reconstructed images for multicenter clinical studies using SPECT techniques.

Differences in the spatial resolution have to be assessed when comparing SPECT images acquired from different SPECT systems, because the differences in the spatial resolution causes different quantitative values due to the partial volume effect [20]. Hoffman 3D phantoms [21] was utilized to assess and to compensate for the different spatial resolution in the cerebral FDG uptake images acquired at different institutions using different PET systems on healthy volunteers [20]. The Iida brain phantom is also useful to evaluate and equalize the spatial resolution of SPECT images obtained from different sites and probably better suited to SPECT, due to its importance in the determination of head contour in SPECT scans. Yamauchi et al. [22] demonstrated that equalization of the spatial resolution significantly reduced the inter-institutional variation of the normal database of rest- and acetazolamide-CBF images among three institutions. The Iida brain phantom may be better suited than the 3D Hoffman phantom when one intends to

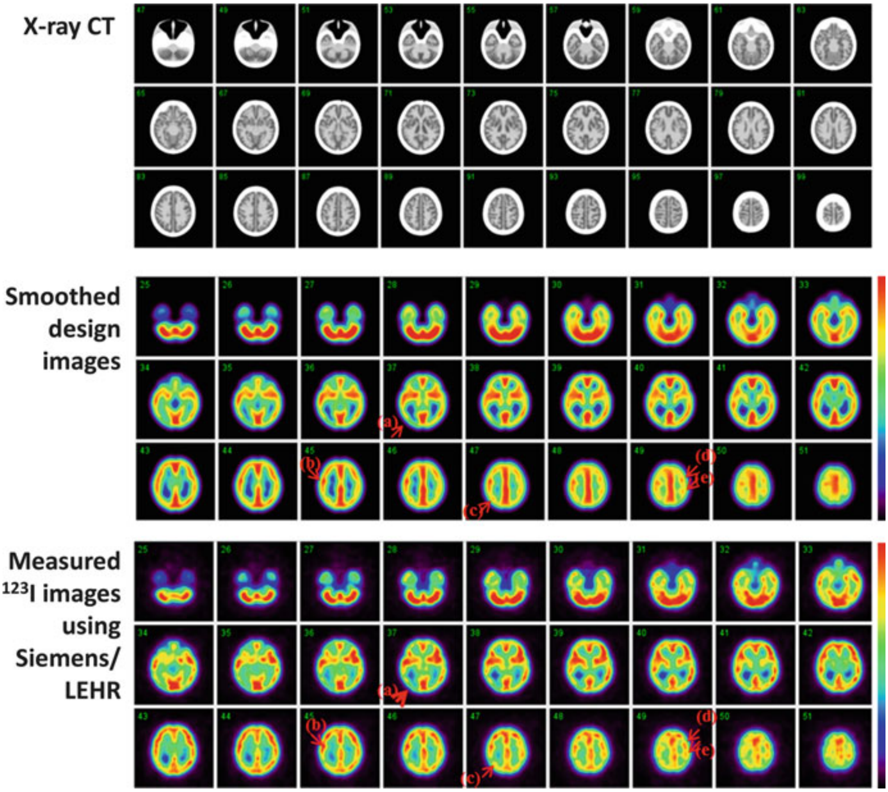

**Fig. 2.5** (*Top*) X-ray CT images of the developed phantom, which contain water and bone-equivalent liquid in the cortical gray matter and bone components of the phantom, (*Middle*) digital design of the gray matter area of the phantom after smoothing with a 16 mm full-width at half maximum Gaussian filter, and (*Bottom*) SPECT images of the phantom filled with $^{123}$I solution in the gray matter compartment and $K_2HPO_4$ solution in the bone compartment. All images are aligned to the digital design. The SPECT images showed good agreement with the digitally designed images. Spots shown with *arrows* (**a**–**e**) demonstrated are examples which indicated good agreement between the digital design and $^{123}$I-SPECT images (Figure is from Iida et al. [19])

assess attenuation or scatter-related variations among different PET/SPECT scanners.

### 2.3.3 Striatum Phantom for Dopamine Transporter Imaging

For dopamine transporter imaging using $^{123}$I-FP-CIT, a phantom simulating the striatum uptake of $^{123}$I-FP-CIT with homogeneous background in the whole brain region (Radiology Support Devices, Long beach, LA, USA) was utilized to evaluate the accuracy and also to calibrate the inter-institutional variations in multicenter evaluations in the EU [23]. The QSPECT reconstruction program was also evaluated using this phantom to assess the accuracy of the specific binding ratio (SBR) values [24], by referring the values calculated from the true radioactivity in the striatum compartments relative to the whole-brain background concentration. Results demonstrated that the SBR values measured using QSPECT software agreed well with those determined from the true radioactivity concentrations. Variation was less than 1/3 of those with FBP reconstruction including the attenuation corrections. This suggested smaller inter-institutional/inter-vendor variations less than 1/3 with QSPECT when compared with FBP. This difference corresponds to the decline of both sensitivity and specificity from 97 to 78 % in our preliminary simulation study. It is therefore of a paramount importance to establish an accurate reconstruction methodology in order to provide a good diagnostic performance in clinical settings. Further careful evaluation is to be carried out.

### *2.3.4 QSPECT Program Packages*

The program package of QSPECT uses a wrapper written in JAVA to run several programs written in C language for Microsoft Windows systems and also includes programs for reconstructing SPECT images, co-registering images, re-slicing, calculating functional images, and printing summary logs. Packages are prepared for the given data processing protocols for the given radiopharmaceuticals. Of those, a package to calculate the rest- and acetazolamide-CBF images with $^{123}$I-IMP and the specific binding ratio (SBR) values with the distribution volume ratio (DVR) images with $^{123}$I-FP-CIT have been utilized to support clinical diagnosis. The programs are also utilized to support clinical research.

## 2.4 Adequacy and Impact in Clinical Scans

### *2.4.1 Dopamine Transporter Function (SBR Quantitation) Using $^{123}$I-FP-CIT*

Figure 2.6 shows an example of an image of a $^{123}$I-FP-CIT scan on a young healthy volunteer (29 years old, male) acquired using a three-head SPECT camera from Toshiba (Tochigi, Japan) fitted with a LHR-fan collimator. The reconstruction was carried out according to Eq. (2.2), which includes the TDCS scatter correction for the geometric projection data and the collimator aperture correction. It can be seen that the head contour was well delineated, as indicated by the red arrows. This is attributed to the carefully designed algorithm: the contour detection with the sine function constraint on the sonogram prior to the scatter correction. With the

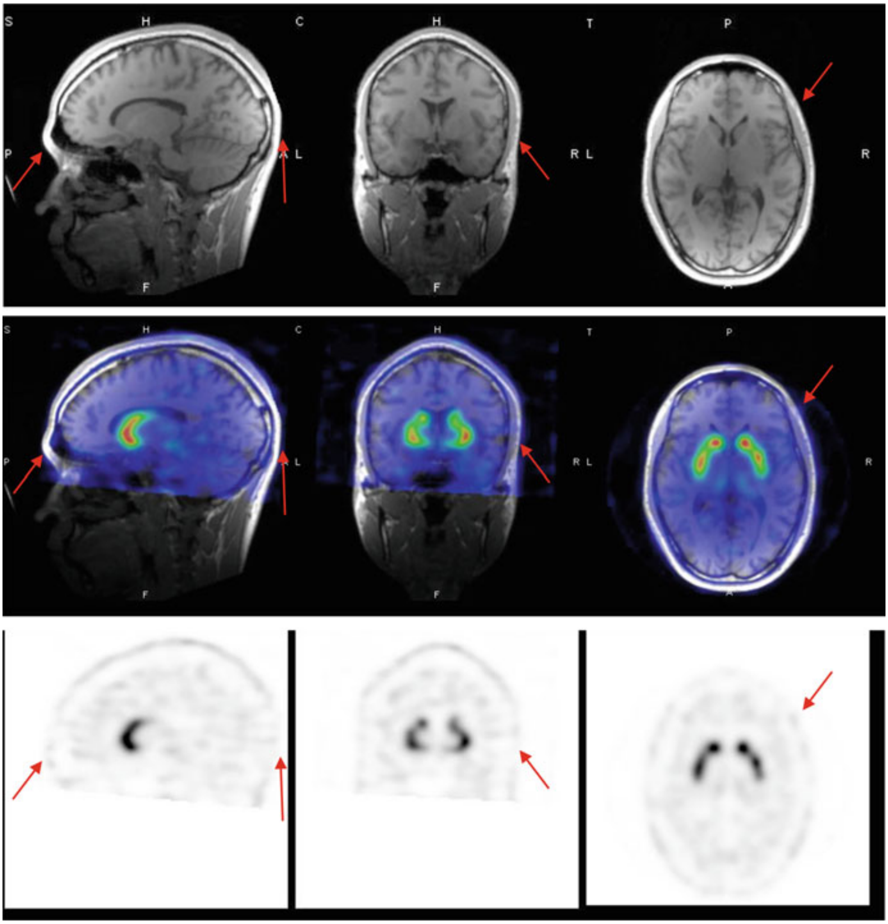

**Fig. 2.6** An example of an image of $^{123}$I-FP-CIT for a healthy 29-year-old male volunteer. The scan was made using the Toshiba 9300R (three-head camera) fitted with an LMEGP-fan collimator. Reconstruction was carried out according to Eq. (2.2) and includes the collimator aperture correction. The head contour is well delineated using the edge detection method implemented in the QSPECT software, as shown with the *red arrows*

improved sensitivity and spatial resolution achieved using the triple head SPECT camera with a fan beam collimator designed for $^{123}$I-nuclides, the collimator aperture model was effective to enhance and provide better striatum-to-background contrast with minimal enhancement of the background noise, though the SBR values essentially remained without changes. There may be lots of application areas where improved image quality can make contributions in clinical settings.

### 2.4.2 Central Benzodiazepine Receptor Imaging Using $^{123}$I-IMZ (Neuron Damage/Residual)

The radiopharmaceutical $^{123}$I-iomazenil (IMZ) is a radiopharmaceutical approved for clinical diagnosis to assess local neuronal damage in patients with epilepsy in Japan. There are also other applications to identify the presence of neuronal damage in the prefrontal areas of patients with neurological deficits after chronic ischemia (or Moyamoya disease) and traumatic brain injuries. We have aimed to highlight significantly damaged areas using $^{123}$I-IMZ and SPECT in such patients by referring to normal patterns by means of 3D-SSP [1] [3, 5]. The challenge is to verify that identical data can be obtained from different SPECT systems installed in different institutions. Consistency is essential in order to utilize a common (normal) database rather than generating separate ones at each institution. At present, we have confirmed that a normal database for $^{123}$I-IMZ generated at two independent institutions installed with different vendor SPECT systems showed smaller variations when QSPECT with AC, SC, and PC was utilized, as compared with vendor FBP reconstruction employing AC only. It was also observed that while vendor reconstruction provided different damage regions with the 3D-SSP analysis using the normal database generated at different institutions, only small differences could be seen between two sets of the normal database with QSPECT reconstruction. This is one area where the standardization of SPECT can make a significant contribution.

### 2.4.3 Rest- and Acetazolamide-CBF Using $^{123}$I-IMP (The Dual-Table Autoradiography Method)

Extensive work has been conducted to establish and validate quantitative assessments of CBF at rest and after administration of acetazolamide with $^{123}$I-IMP and dynamic SPECT using the QSPECT program packages (Fig. 2.7). At present, the QSPECT software packages have been shown to be able to handle the data obtained from most SPECT cameras fitted with parallel beam collimators (see Table 2.1). A total of more than 60,000 scans have been carried out in Japan between 2006 and January 2015, with 16,000 scans in 2014. The scans were mainly to assess the risk of hyper-perfusion after revascularization therapy in patients who are candidates for coronary artery stents and for coronary endarterectomy.

The $^{123}$I-IMP has a high first-pass extraction fraction and is capable of assessing quantitative CBF values for a physiologically wide range of blood flows [25, 26]. The object was to make the quantitative assessment of the rest- and acetazolamide-CBF images from scans obtained in a single session, with two injections of $^{123}$I-IMP at 30 min intervals, to establish the ischemic status in the scans of each patient. A sophisticated compartment model was applied (called dual-table ARG) [27] to make it possible for the stress CBF images to be calculated using table look-up procedures without the need for image subtraction. This method

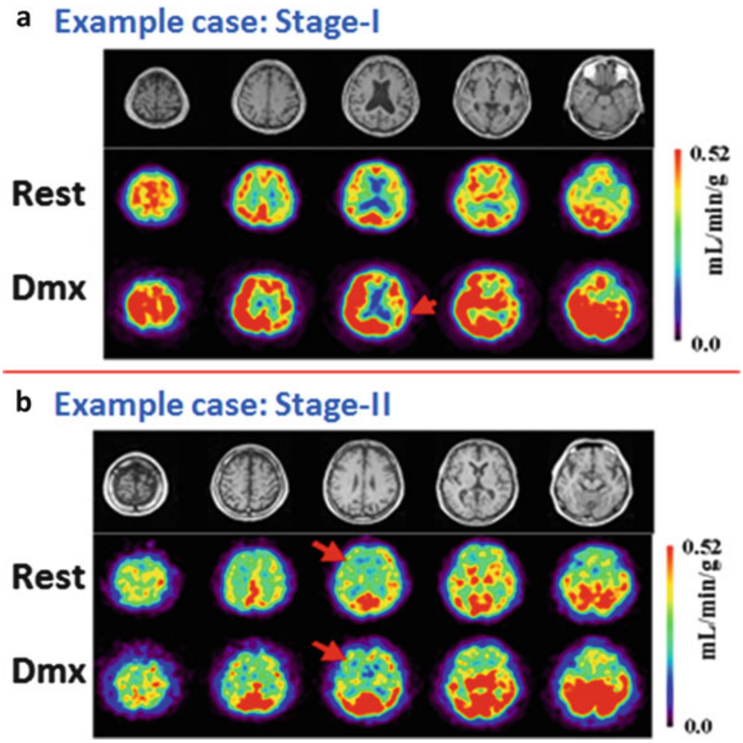

**Fig. 2.7** MR and CBF images at rest and after acetazolamide stress assessed with $^{123}$I-IMP and the dual-table ARG method on two typical low-risk patients (stage I) and a patient with high-risk (stage II) ischemia (Figure is from Iida et al. [28])

appeared not to result in increases in statistical noise and more importantly was able to provide quantitative CBF images with minimal errors and only little inconsistency between the rest- and acetazolamide-CBF assessments. A number of studies were carried out to verify the method in clinical settings, funded by the Ministry of Health, Labour and Welfare Research Foundation from the year of 2007 for 3 years as follows:

(a) There was a fairly good intra-institutional reproducibility of rest- and acetazolamide-CBF images for the same patient, approximately 10 % with 44 patients at nine institutions [28].
(b) Inter-institutional reproducibility of rest- and acetazolamide-CBF images was approximately 6 % in nine patients on 18 data points [29]. An example case is shown in Fig. 2.8.
(c) Consistent results for rest and acetazolamide CBF at rest and after acetazolamide in healthy volunteers among three institutions (a total of 32 healthy volunteers) [22].
(d) Agreement with PET scan results both on relative distribution and absolute values was shown in one institution for five patients [28].

**Table 2.1** List of SPECT camera (3/8 NaI scintillator) and collimator combinations to which QSPECT can be applied. TDCS parameters have been defined for those systems prior to the first clinical examination

| | SPECT camera | | Collimator |
|---|---|---|---|
| Toshiba | GCA-9300 | 3/8inch | N2(LEHR fan), N1(LESHR fan). LEHR para |
| | GCA-7200 | | N2(LEHR fan), N1 (LESHR fan), LEHR para |
| | | | LEGP para |
| | ECAM | | N2(LEHR fan), LMEGP para |
| | Symbia | | LMEGP para |
| Siemens | ECAM | 3/8inch | LEHR para, LMEGP para |
| | Symbia | | LEHR para, LMEGP para |
| GE | Millennium VG | 3/8inch | LEGP para, LEHR para |
| | Infinia | | ELEGP para, LEHR para |
| Hitachi (Philips) | ADAC forte JET stream Philips BrightView Philips SKYLight | 3/8inch | VXGP para |
| | | | CHR para, LEHR para, MEGP para |
| | | | LEGP para, MEGP para, VXHR para |
| Shimazu (Picker ADAC) | IRIX | 3/8inch | LEGP para, LEHR para |
| | AXIS | | LEGP para |
| | PRISM2000 | | LEHR para |
| | PRISM3000 | | LEGP para, LEHR para |

This examination is one good example that demonstrates the contribution of quantitative SPECT in clinical settings. Results of 3D-SSP shown in Fig. 2.8 are helpful in understanding the severity of ischemia and the risk status in patients with major artery occlusion or stenosis. This would also contribute to evaluate a number of therapeutic trials in the future.

## 2.5 Quality Control of the SPECT Scanner

It must be noted that standardization of the quantitative SPECT examination requires detailed self-defined protocols, including for the procedures of the administration, blood sampling, instructions to patients and patient movement, QC of SPECT devices, SPECT acquisition workflow, data pre-processing, and QSPECT reconstruction. Active feedback to deal with possible adverse events related to above procedures at clinical institutions appeared to be effective to maintain the reliability of the clinical scan findings. From July 2009 till May 2011, 139 cases were defined as potentially posing problems or possibly resulting in adverse events

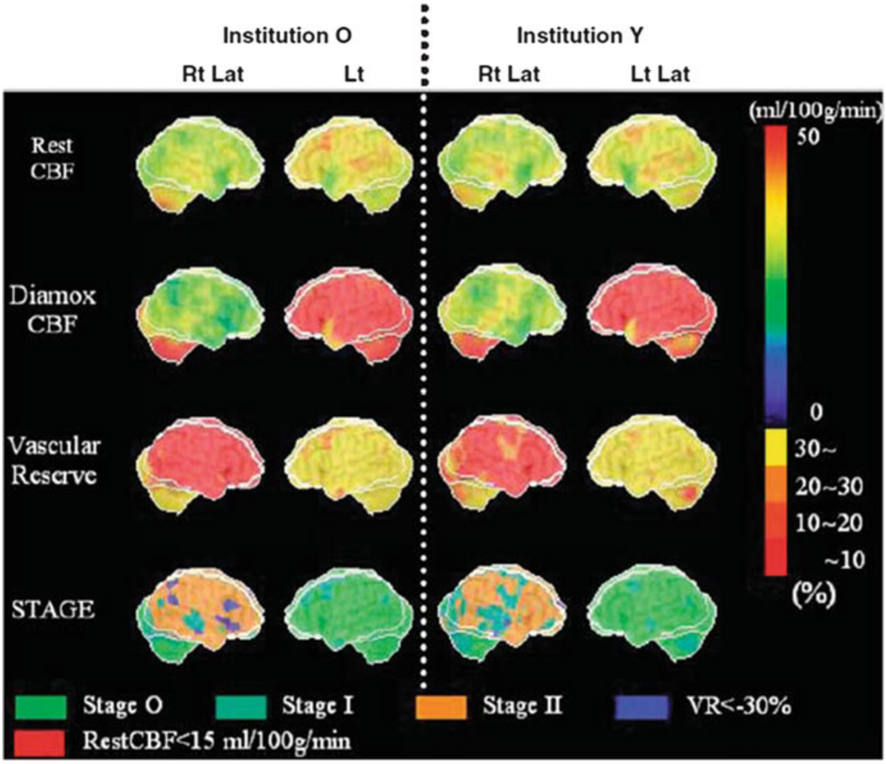

**Fig. 2.8** Stereotactic extraction estimates based on the JET study (SEE-JET) images [4] of a patient obtained in institutions O and Y. The Rt Lat and Lt Lat indicate the right and left hemisphere outer lateral images, respectively. Cerebral blood flow at rest (rest CBF), CBF after the acetazolamide challenge (Diamox CBF), the cerebrovascular reserve (vascular reserve), and severity of hemodynamic cerebral ischemia (STAGE) are shown as three-dimensional cerebral surface images. Images are almost visually identical, from institutions O and Y (Figure is from Yoneda et al. [29])

at 67 institutions. Claims were mostly unexpected low CFR values or unexpectedly low or high absolute CBF values. The software package was designed to keep a record of the complete calculation process, and among the data obtained in this manner, the tissue time-activity curve (tTAC) analysis for sequential short frame dynamic images and dynamic projections appeared to be helpful to identify the sources of errors. Of the 139 cases identified, 64 (42 %) did not suggest errors in the data or in the calculation process, as the observed CFR or small CBF values could be confirmed from results of the tTAC analysis, both in the dynamic reconstructed images as well as in the projection data. In other studies, the tTAC analysis was able to identify errors in the blood radioactivity concentrations ($n = 26$), in the cross calibration procedures ($n = 25$), in the IMP administration ($n = 17$) due to the patient motion ($n = 11$), and other factors including insufficient SPECT QC ($n = 11$). Errors in the software program were not identified in any of the studies.

The feedback provided in the information to the clinical institution was evaluated to be effective to improve the quality of the examination results.

It is possible that the quality of reconstructed SPECT images is degraded by inaccurate reconstruction parameter settings in relation to the attenuation coefficients, accuracy of the head contour determination, inefficient statistical treatment, and also poor quality control (QC) of the SPECT device. It should be noted that there are no standard guidelines (like the NEMA standard) for reconstructed SPECT images, only for projection data. One contribution of the QSPECT reconstruction package is the ability to evaluate the image quality and accuracy on one domain with different systems. It was apparent that the engineers at the vendors should be encouraged to make effort to improve the quality of the reconstructed images rather than only on the projection data. Active feedback to the users at the clinical institutions is also essential to improve the quality of the examination in the quantitation. We also considered the FBP reconstruction with the scatter correction of Chang, for the scatter corrected-projection with TEW would be another possibility for standardization among different institutions. Systematic study has to be coordinated to validate the technique in multicenter settings.

## 2.6 Summary and Future Directions

The QSPECT package is able to reconstruct quantitative tomographic images from projection data acquired using commercial SPECT equipment. The adequacy was demonstrated with a series of phantom experiments. More importantly, the adequacy of images of biological functions and the use of stereotactic statistical analysis software were shown for some protocols in patient populations. Overall, this suggests the adequacy of using clinical SPECT devices for multicenter clinical studies. It is also possible to encourage the use of quantitative reconstruction with diagnosis-assisting software in clinical settings; this would enable an extension of the contribution of SPECT in evaluations of disease severity and so assist in decision making. Further systematic work should be designed to prove this concept for the various tracers in the various clinical settings.

# References

1. Minoshima S, Frey KA, Koeppe RA, Foster NL, Kuhl DE. A diagnostic approach in Alzheimer's disease using three-dimensional stereotactic surface projections of fluorine-18-FDG PET. J Nucl Med. 1995;36(7):1238–48. Epub 1995/07/01.
2. Minoshima S, Giordani B, Berent S, Frey KA, Foster NL, Kuhl DE. Metabolic reduction in the posterior cingulate cortex in very early Alzheimer's disease. Ann Neurol. 1997;42(1):85–94. Epub 1997/07/01.
3. Mizumura S, Kumita S, Cho K, Ishihara M, Nakajo H, Toba M, et al. Development of quantitative analysis method for stereotactic brain image: assessment of reduced accumulation in extent and severity using anatomical segmentation. Ann Nucl Med. 2003;17(4):289–95. Epub 2003/08/23.
4. Mizumura S, Nakagawara J, Takahashi M, Kumita S, Cho K, Nakajo H, et al. Three-dimensional display in staging hemodynamic brain ischemia for JET study: objective evaluation using SEE analysis and 3D-SSP display. Ann Nucl Med. 2004;18(1):13–21. Epub 2004/04/10.
5. Ishii K, Kono AK, Sasaki H, Miyamoto N, Fukuda T, Sakamoto S, et al. Fully automatic diagnostic system for early- and late-onset mild Alzheimer's disease using FDG PET and 3D-SSP. Eur J Nucl Med Mol Imaging. 2006;33(5):575–83. Epub 2006/02/14.
6. Ichihara T, Ogawa K, Motomura N, Kubo A, Hashimoto S. Compton scatter compensation using the triple-energy window method for single- and dual-isotope SPECT. J Nucl Med. 1993;34(12):2216–21. Epub 1993/12/01.
7. Kadrmas DJ, Frey EC, Karimi SS, Tsui BM. Fast implementations of reconstruction-based scatter compensation in fully 3D SPECT image reconstruction. Phys Med Biol. 1998;43 (4):857–73. Epub 1998/05/08.
8. Sohlberg A, Watabe H, Iida H. Acceleration of Monte Carlo-based scatter compensation for cardiac SPECT. Phys Med Biol. 2008;53(14):N277–85. Epub 2008/06/25.
9. Meikle SR, Hutton BF, Bailey DL. A transmission-dependent method for scatter correction in SPECT. J Nucl Med. 1994;35(2):360–7.
10. Narita Y, Eberl S, Iida H, Hutton BF, Braun M, Nakamura T, et al. Monte Carlo and experimental evaluation of accuracy and noise properties of two scatter correction methods for SPECT. Phys Med Biol. 1996;41(11):2481–96.
11. Iida H, Eberl S. Quantitative assessment of regional myocardial blood flow with thallium-201 and SPECT. J Nucl Cardiol. 1998;5(3):313–31.
12. Narita Y, Iida H, Eberl S, Nakamura T. Monte Carlo evaluation of accuracy and noise properties of two scatter correction methods for $^{201}$Tl cardiac SPECT. IEEE Trans Nucl Sci. 1997;44:2465–72.
13. Iida H, Narita Y, Kado H, Kashikura A, Sugawara S, Shoji Y, et al. Effects of scatter and attenuation correction on quantitative assessment of regional cerebral blood flow with SPECT. J Nucl Med. 1998;39(1):181–9.
14. Hirano Y, Koshino K, Watabe H, Fukushima K, Iida H. Monte Carlo estimation of scatter effects on quantitative myocardial blood flow and perfusable tissue fraction using 3D-PET and (15)O-water. Phys Med Biol. 2012;57(22):7481–92. Epub 2012/10/30.
15. Chang L. A method for attenuation correction in radionuclide computed tomography. IEEE Trans Nucl Sci. 1978;25:638–43.
16. Frey EC, Tsui BMW. Collimator-detector response compensation in SPECT. In: Zaidi H, editor. Quantitative analysis in nuclear medicine imaging. Singapore: Springer US; 2006. p. 141–66.
17. Hapdey S, Soret M, Ferrer L, Koulibaly P, Henriques J, Bardiès M, et al. Quantification in SPECT: myth or reality ? A multicentric study. IEEE Nucl Sci Symp Conf Rec. 2004;5 (3):3170–317.
18. Sohlberg A, Watabe H, Iida H. Three-dimensional SPECT reconstruction with transmission-dependent scatter correction. Ann Nucl Med. 2008;22(7):549–56. Epub 2008/08/30.

19. Iida H, Hori Y, Ishida K, Imabayashi E, Matsuda H, Takahashi M, et al. Three-dimensional brain phantom containing bone and grey matter structures with a realistic head contour. Ann Nucl Med. 2013;27(1):25–36.
20. Joshi A, Koeppe RA, Fessler JA. Reducing between scanner differences in multi-center PET studies. NeuroImage. 2009;46(1):154–9. Epub 2009/05/22.
21. Hoffman EJ, Cutler PD, Digby WM, Mazziotta JC. 3-D phantom to simulate cerebral blood flow and metabolic images for PET. IEEE Trans Nucl Sci. 1990;37:616–20.
22. Yamauchi M, Imabayashi E, Matsuda H, Nakagawara J, Takahashi M, Shimosegawa E, et al. Quantitative assessment of rest and acetazolamide CBF using quantitative SPECT reconstruction and sequential administration of (123)I-iodoamphetamine: comparison among data acquired at three institutions. Ann Nucl Med. 2014;28(9):836–50. Epub 2014/07/09.
23. Tossici-Bolt L, Dickson JC, Sera T, de Nijs R, Bagnara MC, Jonsson C, et al. Calibration of gamma camera systems for a multicentre European $^{123}$I-FP-CIT SPECT normal database. Eur J Nucl Med Mol Imaging. 2011;38(8):1529–40.
24. Tossici-Bolt L, Hoffmann SM, Kemp PM, Mehta RL, Fleming JS. Quantification of [$^{123}$I]FP-CIT SPECT brain images: an accurate technique for measurement of the specific binding ratio. Eur J Nucl Med Mol Imaging. 2006;33(12):1491–9. Epub 2006/07/22.
25. Iida H, Akutsu T, Endo K, Fukuda H, Inoue T, Ito H, et al. A multicenter validation of regional cerebral blood flow quantitation using [$^{123}$I]iodoamphetamine and single photon emission computed tomography. J Cereb Blood Flow Metab. 1996;16(5):781–93. Epub 1996/09/01.
26. Iida H, Itoh H, Nakazawa M, Hatazawa J, Nishimura H, Onishi Y, et al. Quantitative mapping of regional cerebral blood flow using iodine-123-IMP and SPECT. J Nucl Med. 1994;35 (12):2019–30. Epub 1994/12/01.
27. Kim KM, Watabe H, Hayashi T, Hayashida K, Katafuchi T, Enomoto N, et al. Quantitative mapping of basal and vasareactive cerebral blood flow using split-dose (123)I-iodoamphetamine and single photon emission computed tomography. NeuroImage. 2006;33 (3):1126–35.
28. Iida H, Nakagawara J, Hayashida K, Fukushima K, Watabe H, Koshino K, et al. Multicenter evaluation of a standardized protocol for rest and acetazolamide cerebral blood flow assessment using a quantitative SPECT reconstruction program and split-dose $^{123}$I-iodoamphetamine. J Nucl Med. 2010;51(10):1624–31.
29. Yoneda H, Shirao S, Koizumi H, Oka F, Ishihara H, Ichiro K, et al. Reproducibility of cerebral blood flow assessment using a quantitative SPECT reconstruction program and split-dose 123I-iodoamphetamine in institutions with different gamma-cameras and collimators. J Cereb Blood Flow Metab. 2012;32(9):1757–64.

# Chapter 3
# PET Imaging Innovation by DOI Detectors

**Taiga Yamaya**

**Abstract** Positron emission tomography (PET) plays important roles in cancer diagnosis, neuroimaging, and molecular imaging research. However potential points remain for which big improvements could be made, including spatial resolution, sensitivity, and manufacturing costs. Depth-of-interaction (DOI) measurement in the radiation sensor will be a key technology to get any significant improvement in sensitivity while maintaining high spatial resolution. We have developed four-layered DOI detectors based on our original light-sharing method. DOI measurement also has a potential to expand PET application fields because it allows for more flexible detector arrangement. As an example, we are developing the world's first, open-type PET geometry, "OpenPET," which is expected to lead to PET imaging during treatment. The DOI detector itself continues to evolve with the help of recently developed semiconductor photodetectors, often referred to as silicon photomultipliers (SiPMs). We are developing a SiPM-based DOI detector "X'tal cube" to achieve sub-mm spatial resolution, which is reaching the theoretical limitation of PET imaging. Innovation of SiPMs encourages our development of PET/MRI, which is attracting great notice in terms of smaller radiation exposure and better contract in soft tissues compared with current PET/CT.

**Keywords** PET • Depth-of-interaction • DOI • In-beam PET • Brain PET • SiPM • PET/MRI

## 3.1 Introduction

Positron emission tomography (PET) plays important roles in cancer diagnosis, neuroimaging, and molecular imaging research, but potential points remain for which big improvements could be made, including spatial resolution, sensitivity, and manufacturing costs. For example, the sensitivity of present PET scanners does not exceed 10 %. This means that more than 90 % of the gamma rays emitted from a subject are not utilized for imaging. Therefore, research on next generation PET technologies remains a hot topic worldwide.

---

T. Yamaya (✉)
Molecular Imaging Center, National Institute of Radiological Sciences, Chiba, Japan
e-mail: taiga@nirs.go.jp

Y. Kuge et al. (eds.), *Perspectives on Nuclear Medicine for Molecular Diagnosis and Integrated Therapy*, DOI 10.1007/978-4-431-55894-1_3

The Imaging Physics Team at National Institute of Radiological Sciences (NIRS) has carried out basic studies on radiation detectors, data acquisition systems, image reconstruction algorithms, and data correction methods to improve image quality and quantity in nuclear medicine as well as to explore innovative systems.

A depth-of-interaction (DOI) detector, for which various methods have been studied [1–7], will be a key device to get any significant improvement in sensitivity while maintaining high spatial resolution (Fig. 3.1). In order to maintain enough detection efficiency, the scintillation crystals should be 2–3 cm long. In conventional detectors, the crystal thickness causes uncertainty in position identification, which results in degraded spatial resolution at the peripheral area of a field-of-view. On the other hand, DOI can reduce the parallax error while maintaining the efficiency.

We have developed four-layered DOI detectors based on a light-sharing method [8, 9]. One successful proof of concept was the "jPET" project, in which we developed brain prototype PET with our DOI detectors; almost uniform spatial resolution around 2 mm all over the field-of-view was obtained with iterative image reconstruction with geometrically defined system matrix [10]. We have also succeeded to upgrade the DOI detector to have better spatial resolution with cheaper production costs: successful identification of 32 × 32 × 4 array of LYSO crystals sized in $1.45 \times 1.45 \times 4.5\ \mathrm{mm}^3$ with a 64ch flat panel PMT (H8500, Hamamatsu Photonics K.K., Japan) [11], which has enabled Shimadzu's new products of positron emission mammography.

DOI measurement also has a potential to expand PET application fields because it allows for more flexible detector arrangement. As an example, we are developing the world's first, open-type PET geometry, "OpenPET," which is expected to lead to PET imaging during treatment. In addition, flexible system design of OpenPET

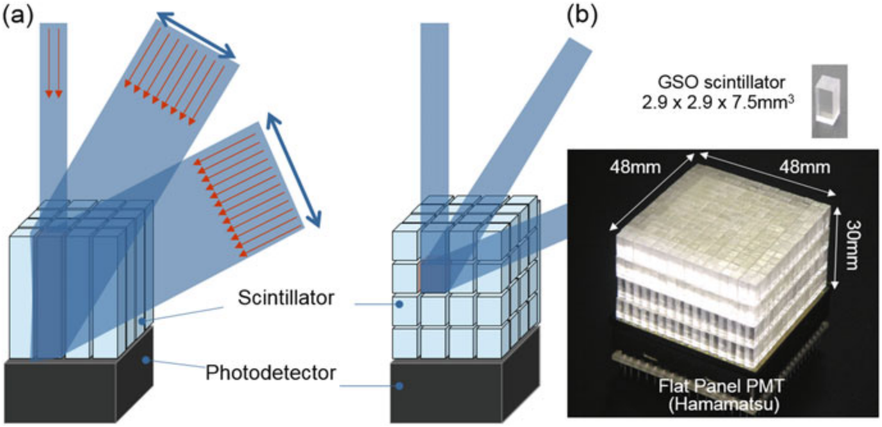

**Fig. 3.1** Comparison between a conventional PET detector (**a**) and our depth-of-interaction (DOI) detector. The DOI detector (**b**) eliminates the parallax error, which is caused by the thickness of crystals in conventional 2D detectors

prototypes is enabling us to develop an innovative brain scanner “helmet-chin PET.” The DOI detector itself continues to evolve with the help of recently developed semiconductor photodetectors, often referred to as silicon photomultipliers (SiPMs). We are developing a SiPM-based DOI detector “X’tal cube” to achieve sub-mm spatial resolution, which is reaching the theoretical limitation of PET imaging. Innovation of SiPMs encourages our development of PET/MRI, which is attracting great notice in terms of smaller radiation exposure and better contract in soft tissues compared with current PET/CT. By using our SiPM-based DOI detectors, we are developing a novel, high-performance, and low-cost brain PET/MRI to meet demands for earlier diagnosis of Alzheimer’s disease. The key concept is a RF coil with DOI PET detectors, which has a potential to upgrade any existing MRI to PET/MRI. In this paper, an overview of above developments is shown.

## 3.2 The OpenPET: A Future PET for Therapy Imaging

OpenPET is our original idea to realize the world’s first open-type 3D PET scanner for PET-image guided particle therapy such as in situ dose verification and direct tumor tracking. The principal of dose verification for particle therapy is based on the measurement of positron emitters which are produced through fragmentation reactions caused by proton or $^{12}$C ion irradiation. Even with a full-ring geometry, the OpenPET has an open gap between its two detector rings through which the treatment beam passes, while conventional positron cameras applied to particle therapy imaging have been basically limited to planar imaging with lower detection efficiency [12–14]. Following our initial proposal of the dual-ring OpenPET (DROP) in 2008 (Fig. 3.2a) [15], we developed a small prototype in 2010 to show a proof of concept (Fig. 3.2b) [16]. In 2011, we also proposed the single-ring OpenPET (SROP), which is more efficient than DROP in terms of manufacturing cost and sensitivity [17]. We developed two small SROP prototypes in 2012 and 2013 (Fig. 3.2d, e) [18, 19], and we succeeded in visualizing a 3D distribution of beam stopping positions inside a phantom with the help of radioactive beams ($^{11}$C beam and $^{10}$C beam) used as primary beams (Fig. 3.2f) [20]. Following these good results, in 2014, we have finally developed a whole-body prototype of DROP (Fig. 3.2g) [21].

The key technology which enabled OpenPET is our original, four-layered DOI detector. In order to measure radiations from the limited activity produced though fragmentation reactions, Zr-doped GSO (GSOZ), which contains less natural radioactivity, was chosen for the scintillators instead of Lu-based scintillators although timing performance was compromised. In order to compensate for the limited light yield, on the other hand, we used 64-channel, flat-panel PMTs with a super-bialkali photocathode (Hamamatsu R10552-100-M64), which had a 30 % higher quantum efficiency [22]. In order to enable stable in-beam PET measurement even under high background radiations, voltage divider circuits were designed so as to have

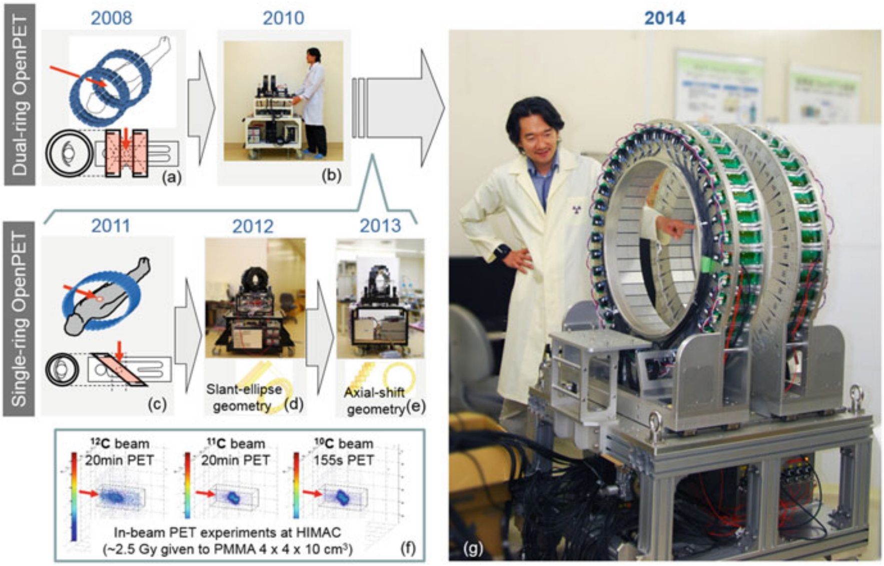

**Fig. 3.2** Conceptual sketches and prototypes of the OpenPET geometries: the dual-ring OpenPET (DROP) (**a**–**b**) and the single-ring OpenPET (**c**–**e**). Following proofs-of-concept of in-beam imaging (**f**), a whole-body DROP was developed (**g**)

five times higher linearity. In order to avoid severe radiation damage, in addition, gain control ASICs were not implemented in the front-end circuits, and position analyzer circuits were placed with a 15-m cable extension. A data acquisition system was developed based on the single events collection.

The prototype consisted of two detector rings, and each detector ring had two subrings of 40 detectors. Each detector consisted of 16 × 16 × 4 array of GSOZ (2.8 × 2.8 × 7.5 mm$^3$). The portable gantry had a compact design; each detector ring had a 940 mm outer diameter and 171 mm thickness for the detector inner bore of 640 mm diameter and 113 mm thickness.

## 3.3 The Helmet-Chin PET for Super High-Sensitive Brain Imaging

For a potential demand for brain molecular imaging, prototypes of brain dedicated PET scanners have been developed. However all previous developments are based on a cylindrical geometry [3, 10, 23–25], which is not the most efficient for brain imaging. Making the detector ring as small as possible is essential in PET, because sensitivity can be increased with a limited number of detectors. With appropriate DOI detectors, which reduce the parallax error caused by the thickness of the scintillators, spatial resolution can be maintained, or even improved by reducing the angular deviation effect. Therefore, we developed the world’s first helmet-chin PET, in which DOI detectors are arranged to form a hemisphere, for compact, high-sensitivity, high-resolution, and low-cost PET imaging [26, 27].

Our basic idea relies on the evidence that the average sensitivity of a hemisphere PET is about 1.5-times higher than that of a cylinder PET of the same radius and height, while surface area is the same for both geometries (Fig. 3.3a, b). In addition, use of 12 % more detectors for “chin detectors,” which are placed like a chin strap, improves sensitivity especially at the central area (Fig. 3.3c). In the prototype, 47 block detectors were used to form a hemisphere of 25 cm inner diameter and 50 cm outer diameter, and seven block detectors were used for the chin strap (Fig. 3.3d). The total number of detectors was about only 1/5 of that to be used in whole body PET. Each detector block was a four-layered DOI detector, which consisted of 1024 Zr-doped GSO crystals (2.8 mm × 2.8 mm × 7.5 mm) and a high-sensitivity type of 64-channel flat-panel PMT. The data acquisition system was

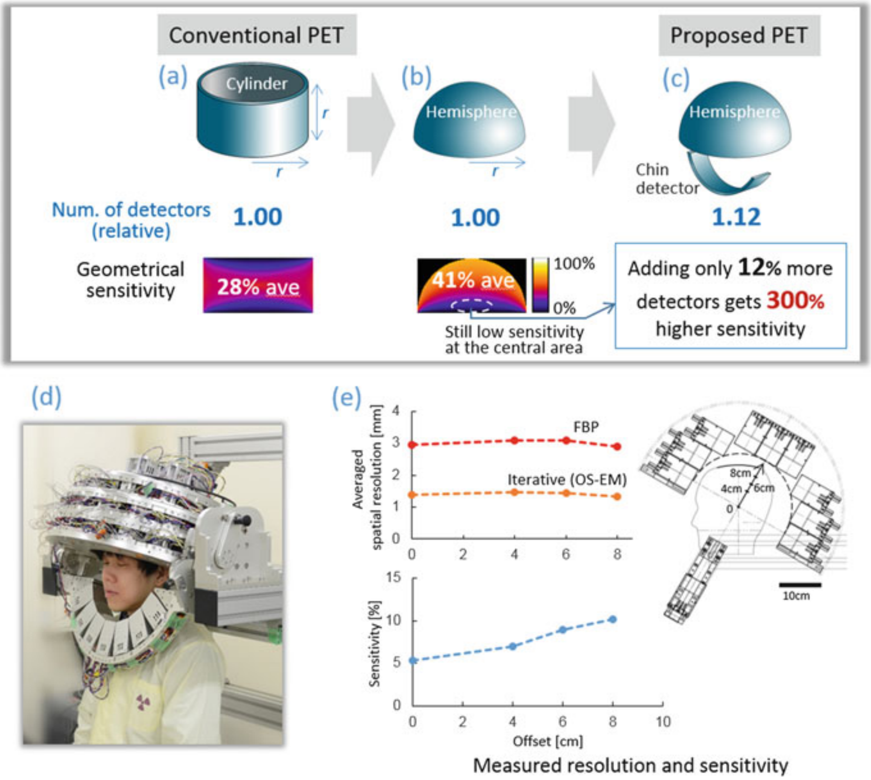

**Fig. 3.3** Comparison between a conventional cylinder PET (**a**) and the proposed helmet-chin PET (**b, c**); the hemisphere detector arrangement obtains 1.5 times higher sensitivity, and adding only 12 % more detectors gets three times higher sensitivity at the central area. A prototype of the helmet-chin PET (**d**) succeeded in obtaining excellent sensitivity and resolution performance (**e**)

developed based on single event collection. An iterative reconstruction method with detector modeling was applied.

Measured sensitivity was 5 % at the cerebellum region and 10 % at the parietal region for a standard 400–600 keV energy window. Averaged FWHM of point sources was 3.0 mm (FBP) and 1.4 mm (iterative) (Fig. 3.3e).

## 3.4 The X'tal Cube: 0.8 mm Isotropic Resolution, a World Record

X'tal (crystal) cube is a future DOI detector we are developing. SiPMs, multi-pixel photon counters (MPPCs), are coupled on all sides of a scintillation crystal block, which is segmented into a 3D array of cubes [28] (Fig. 3.4a). Crystal segmentation is made by irradiating a laser to a monolithic crystal (Fig. 3.4b) [29]. No reflector is inserted into the crystal block so that scintillation light originating in one of the cubic segment spreads 3-dimensionally and distributes among all MPPCs on the crystal block. In 2012, we achieved 1-mm cubic resolution with 18 × 18 × 18 segments made by 3D laser processing (Fig. 3.4c, d) [30, 31]. In the last year, we succeeded in identifying $(0.8\ \text{mm})^3$ crystal segments, which is a world record [32].

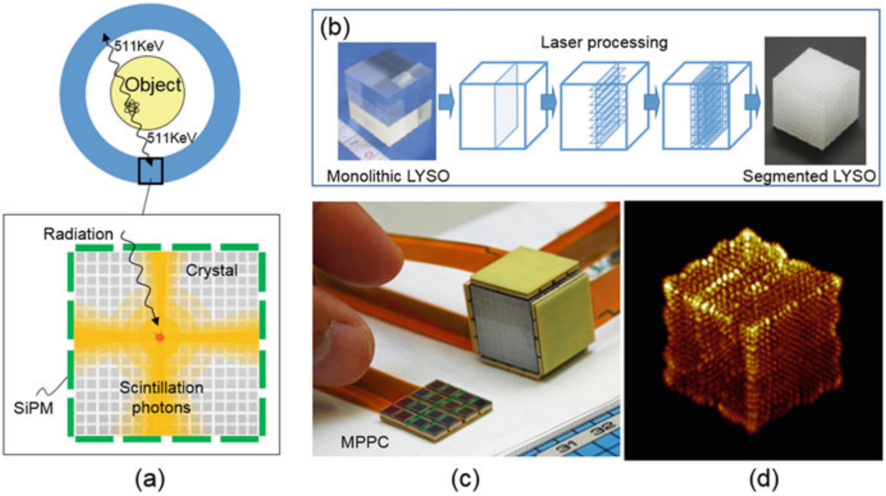

**Fig. 3.4** Conceptual sketch of the X'tal cube (**a**) and a prototype X'tal cube detector (**c**) with a monolithic crystal block segmented by the 3D laser processing (**b**). A flood histogram shows position identification performance of 18 × 18 × 18 array of 1 $\text{mm}^3$ crystal segments (**d**)

## 3.5 The Add-On PET: A PET Insert to Upgrade Existing MRI to PET/MRI

One of the major innovations made in recent years is combined PET/MRI (Fig. 3.5a) [33–46], but utilization of DOI measurement in PET detectors has not been studied well. DOI measurement, which allows for use of a smaller detector ring, is essential for PET in order to exploit the excellent potentials of PET imaging in terms of improved spatial resolution and sensitivity as well as reduced production costs of PET instrument. Therefore we proposed a new combined PET/MRI that makes full use of DOI measurement (Fig. 3.5b) [47, 48].

In order to make a PET detector ring as small as possible while placing electronic parts such as photodetectors and front-end circuits outside of a RF coil, PET detector modules were placed between spokes of the birdcage RF coil (Fig. 3.5c). For each detector module, electronic parts were covered with a Cu shielding box with a hole in front of the photodetectors, and scintillators were sticking out of the shielding box to allow their placement inside of the birdcage coil (Fig. 3.5e). In theory, the proposed birdcage coil integrated with PET detectors can be applied to any existing MRI as an additional choice of RF coils. For a proof of

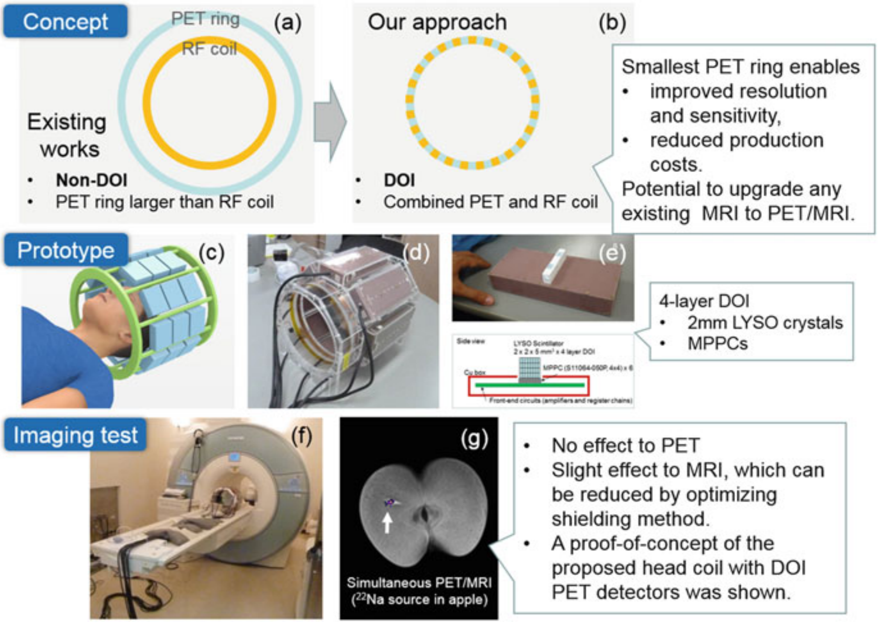

**Fig. 3.5** Concept comparison between conventional PET/MRI (**a**) and the proposed add-on PET/MRI (**b**). A prototype (**c, d**) combined with DOI detector modules (**e**) was applied to 3T MRI (**f**) to demonstrate simultaneous PET/MRI imaging (**g**)

concept, we developed a full-ring prototype (four-layered arrays of 2.0 mm-LYSO with MPPCs) (Fig. 3.5d), which was applied to a 3T MRI (MAGNETOM Verio, Siemens) (Fig. 3.5f).

After evaluating interference between PET and MRI, no undesirable effect was seen in the PET imaging in terms of energy resolution and position identification. While a uniform static magnetic field was obtained, about a 20 % decrease in signal-to-noise ratio was observed in MR images; we suspected this was due to noise contamination from outside the MRI room. Although further optimization is required for shielding, we demonstrated a proof of concept of the proposed head coil with DOI PET detectors (Fig. 3.5g).

## 3.6 Conclusions

In PET, DOI measurement is a key technology to get significant improvement in sensitivity while maintaining high spatial resolution. DOI measurement also has a potential to expand PET application fields because it allows for more flexible detector arrangement. In this paper, two current developments, the OpenPET toward PET-image guided particle therapy and the helmet-chin PET for high-sensitive brain imaging, were shown. Current development status of the next-generation DOI detector X'tal cube, which uses SiPMs as a photosensor, was also described. SiPM-based DOI detector enabled the add-on PET, which is a PET insert having a potential to upgrade existing MRI to PET/MRI.

**Acknowledgments** The author would like to acknowledge the support of all research members engaged in the OpenPET project, the helmet-chin PET project, the X'tal cube project, and the add-on PET project. The OpenPET project was partially supported by the Grant-in-Aid for Scientists Research (A) of Kakenhi (22240065 and 25242052). The helmet-chin PET project was partially supported by ATOX Co., Ltd. (Tokyo, Japan). The X'tal cube project was partially supported by the Japan Science and Technology Agency (JST). The add-on PET project was partially supported by the JST and the Japan Agency for Medical Research and Development (AMED).

## References

1. Carrier C, Martel C, Schmitt D, Leconte R. Design of a high resolution positron emission tomograph using solid state scintillation detectors. IEEE Trans Nucl Sci. 1988;35:685–90.
2. Yamamoto S, Ishibashi H. A GSO depth of interaction detector for PET. IEEE Trans Nucl Sci. 1998;45:1078–82.
3. Wienhard K, Schmand M, Casey ME, Baker K, Bao J, Eriksson L, et al. The ECAT HRRT: performance and first clinical application of the new high-resolution research tomograph. IEEE Trans Nucl Sci. 2002;49:104–10.
4. Yamashita T, Watanabe M, Shimizu K, Uchida H. High resolution block detectors for PET. IEEE Trans Nucl Sci. 1990;37:589–93.
5. Moses WW, Derenzo SE, Melcher CL, Manente RA. A room temperature LSO/PIN photodiode PET detector module that measures depth of interaction. IEEE Trans Nucl Sci. 1995;42:1085–9.
6. Miyaoka RS, Lewellen TK, Yu H, McDaniel DL. Design of a depth of interaction (DOI) PET detector module. IEEE Trans Nucl Sci. 1998;45:1069–73.
7. Shao Y, Silverman RW, Farrell R, Cirignano L, Grazioso R, Shah KS, et al. Design studies of a high resolution PET detector using APD arrays. IEEE Trans Nucl Sci. 2000;47:1051–7.
8. Murayama H, Ishibachi H, Uchida H, Omura T, Yamashita T. Depth encoding multicrystal detectors for PET. IEEE Trans Nucl Sci. 1998;45:1152–7.
9. Inadama N, Murayama H, Omura T, Yamashita T, Yamamoto S, Ishibashi H, et al. A depth of interaction detector for PET with GSO crystals doped with different amounts of Ce. IEEE Trans Nucl Sci. 2002;49:629–33.
10. Yamaya T, Yoshida E, Obi T, Ito H, Yoshikawa K, Murayama H. First human brain imaging by the jPET-D4 prototype with a pre-computed system matrix. IEEE Trans Nucl Sci. 2008;55:2482–92.
11. Tsuda T, Murayama H, Kitamura K, Yamaya T, Yoshida E, Omura T, et al. A four-layer depth of interaction detector block for small animal PET. IEEE Trans Nucl Sci. 2004;51:2537–42.
12. Pawelke J, Byars L, Enghardt W, Fromm WD, Geissel H, Hasch BG, et al. The investigation of different cameras for in-beam PET imaging. Phys Med Biol. 1996;41:279–96.
13. Iseki Y, Mizuno H, Futami Y, Tomitani T, Kanai T, Kanazawa M, Kitagawa A, Murakami T, Nishio T, Suda M. Positron camera for range verification of heavy-ion radiotherapy. Nucl Inst Methods Phys Res A. 2003;515:840–9.
14. Nishio T, Ogino T, Nomura K, Uchida H. Dose-volume delivery guided proton therapy using beam on-line PET system. Med Phys. 2006;33:4190–7.
15. Yamaya T, Inaniwa T, Minohara S, Yoshida E, Inadama N, Nishikido F, et al. A proposal of an open PET geometry. Phys Med Biol. 2008;53:757–73.
16. Yamaya T, Yoshida E, Inaniwa T, Sato S, Nakajima Y, Wakizaka H, et al. Development of a small prototype for a proof-of-concept of OpenPET imaging. Phys Med Biol. 2011;56:1123–37.
17. Tashima H, Yamaya T, Yoshida E, Kinouchi S, Watanabe M, Tanaka E. A single-ring OpenPET enabling PET imaging during radiotherapy. Phys Med Biol. 2012;57:4705–18.
18. Yoshida E, Tashima T, Wakizaka H, Nishikido F, Hirano Y, Inadama N, et al. Development of a single-ring OpenPET prototype. Nucl Inst Methods Phys Res A. 2013;729:800–8.
19. Yamaya T, Yoshida E, Tashima H, Nakajima Y, Nishikido F, Hirano Y, et al. A prototype of a novel transformable single-ring OpenPET. In: IEEE nuclear science symposium conference record. Piscataway: IEEE; 2013. M07-1.
20. Urakabe E, Kanai T, Kanazawa M, Kitagawa A, Noda K, Tomitani T, et al. Spot scanning using radioactive $^{11}$C beams for heavy-ion radiotherapy. Jpn J Appl Phys. 2001;40:2540–8.
21. Yamaya T, Yoshida E, Tashima H, Inadama N, Nishikido F, Hirano Y, et al. Whole-body dual-ring OpenPET for in-beam particle therapy imaging. In: IEEE nuclear science symposium conference record. Piscataway: IEEE; 2014. M15-8.

22. Hirano Y, Nitta M, Inadama N, Nishikido F, Yoshida E, Murayama H, et al. Performance evaluation of a depth-of-interaction detector by use of position-sensitive PMT with a super-bialkali photocathode. Radiol Phys Technol. 2014;7:57–66.
23. Yamamoto S, Honda M, Oohashi T, Shimizu K, Senda M. Development of a brain PET system, PET-Hat: a wearable PET system for brain research. IEEE Trans Nucl Sci. 2011;58:668–73.
24. Majewski S, Proffitt J, Brefczynski-Lewis J, Stolin A, Weisenberger AG, Xi W, et al. HelmetPET: a silicon photomultiplier based wearable brain imager. In: IEEE nuclear science symposium conference record. Piscataway: IEEE; 2011. p. 4030–4.
25. Omura T, Moriya T, Yamada R, Yamauchi H, Saito A, Sakai T. Development of a high-resolution four-layer DOI detector using MPPCs for brain PET. In: IEEE nuclear science symposium conference record. 2012. p. 3560–3.
26. Tashima H, Ito H, Yamaya T. A proposed helmet-PET with a jaw detector enabling high-sensitivity brain imaging. In: IEEE nuclear science symposium conference record. 2013. M11-11.
27. Yamaya T, Yoshida E, Tashima H, Inadama N, Shinaji T, Wakizaka H, et al. First prototype of a compact helmet-chin PET for high-sensitivity brain imaging. J Nucl Med. 2015;56:317.
28. Yamaya T, Mitsuhashi T, Matsumoto T, Inadama N, Nishikido F, Yoshida E, et al. A SiPM-based isotropic-3D PET detector X'tal cube with a three-dimensional array of 1 mm3 crystals. Phys Med Biol. 2011;56:6793–807.
29. Moriya T, Fukumitsu K, Sakai T, Ohsuka S, Okamoto T, Takahashi H, et al. Development of PET detectors using monolithic scintillation crystals processed with sub-surface laser engraving technique. IEEE Trans Nucl Sci. 2010;57:2455–9.
30. Yoshida E, Hirano Y, Tashima H, Inadama N, Nishikido F, Moriya T, et al. Impact of the laser-processed X'tal cube detector on PET imaging in a one-pair prototype system. IEEE Trans Nucl Sci. 2013;60:3172–80.
31. Yoshida E, Tashima H, Hirano Y, Inadama N, Nishikido F, Muraya H, et al. Spatial resolution limits for the isotropic-3D PET detector X'tal cube. Nucl Inst Methods Phys Res A. 2013;728:107–11.
32. Munetaka N, Inadama N, Hirano Y, Nishikido F, Yoshida E, Tashima H, et al. The X'tal cube PET detector of isotropic (0.8 mm)$^3$ crystal segments. In: IEEE nuclear science symposium conference record. 2014. M04-1.
33. Shao Y, Cherry S. Simultaneous PET and MR imaging. Phys Med Biol. 1997;42:1965–70.
34. Slates RB, Farahani K, Shao Y, Marsden PK, Taylor J, Summers PE, et al. A study of artefacts in simultaneous PET and MR imaging using a prototype MR compatible PET scanner. Phys Med Biol. 1999;44:2015–27.
35. Catana C, Wu Y, Judenhofer MS, Qi J, Pichler BJ, Cherry SR. Simultaneous acquisition of multislice PET and MR images: initial results with a MR-compatible PET scanner. J Nucl Med. 2006;47:1968–76.
36. Pichler BJ, Judenhofer MS, Catana C, Walton JH, Kneilling M, Nutt RE, et al. Performance test of an LSO-APD detector in a 7-T MRI scanner for simultaneous PET/MRI. J Nucl Med. 2006;47:639–47.
37. Schlyer D, Vaska P, Tomasi D, Woody C, Maramraju S-H, Southekal S, et al. A simultaneous PET/MRI scanner based on RatCAP in small animals. In: IEEE nuclear science symposium conference record. 2007. p. 3256.
38. Schlemmer HP, Pichler BJ, Schmand M, Burbar Z, Michel C, Ladebeck R, et al. Simultaneous MR/PET imaging of the human brain: feasibility study. Radiology. 2008;248:1028–35.
39. Yamamoto S, Hatazawa J, Imaizumi M, Shimosegawa E, Aoki M, Sugiyama E, et al. A multi-slice dual layer MR-compatible animal PET system. IEEE Trans Nucl Sci. 2009;56:2706–13.
40. Yamamoto S, Imaizumi M, Kanai Y, Tatsumi M, Aoki M, Sugiyama E, et al. Design and performance from an integrated PET/MRI system for small animals. Ann Nucl Med. 2010;24:89–98.

41. Kwon SI, Lee JS, Yoon HS, Ito M, Ko GB, Choi JY, et al. Development of small-animal PET prototype using silicon photomultiplier (SiPM): initial results of phantom and animal imaging studies. J Nucl Med. 2011;52:572–9.
42. Maramraju SH, Smith SD, Junnarkar SS, Schulz D, Stoll S, Ravindranath B, et al. Small animal simultaneous PET/MRI: initial experiences in a 9.4 T microMRI. Phys Med Biol. 2011;56:2459–80.
43. Zaidi H, Ojha N, Morich M, Griesmer J, Hu Z, Maniawski P, et al. Design and performance evaluation of a whole-body ingenuity TF PET-MRI system. Phys Med Biol. 2011;56:3091–106.
44. Delso G, Fürst S, Jakoby B, Ladebeck R, Ganter C, Nekolla SG, et al. Performance measurements of the Siemens mMR integrated whole-body PET/MR scanner. J Nucl Med. 2011;52:1914–22.
45. Yoon HS, Ko GB, Kwon SI, Lee CM, Ito M, Chan Song I, et al. Initial results of simultaneous PET/MRI experiments with an MRI-compatible silicon photomultiplier PET scanner. J Nucl Med. 2012;53:608–14.
46. Lee B J, Grant A M, Chang C-M, Levin C S. MRI measurements in the presence of a RF-penetrable PET insert for simultaneous PET/MRI. Abstract Book of 2015 World Molecular Imaging Congress. 2015. SS 126.
47. Nishikido F, Obata T, Shimizu K, Suga M, Inadama N, Tachibana A, et al. Feasibility of a brain-dedicated PET-MRI system using four-layer detectors integrated with an RF head coil. Nucl Instr Methods A. 2014;756:6–13.
48. Nishikido F, Tachibana A, Obata T, Inadama N, Yoshida E, Suga M, et al. Development of 1.45-mm resolution four-layer DOI–PET detector for simultaneous measurement in 3T MRI. Radiol Phys Technol. 2015;8:111–9.

# Chapter 4
# Semiconductor Detector-Based Scanners for Nuclear Medicine

**Wataru Takeuchi, Atsuro Suzuki, Yuichiro Ueno, Tohru Shiga,
Kenji Hirata, Shozo Okamoto, Songji Zhao, Yuji Kuge, Naoki Kubo,
Kentaro Kobayashi, Shiro Watanabe, Keiji Kobashi, Kikuo Umegaki,
and Nagara Tamaki**

**Abstract** Semiconductor detectors have the potential to improve the quantitative accuracy of nuclear medicine imaging with their better energy and intrinsic spatial resolutions than those of conventional scintillator-based detectors. The fine energy resolution leads to a better image contrast due to better scatter rejection. The fine intrinsic spatial resolution due to a pixelated structure leads to a better image contrast and lower partial volume effect. Their pixelated structures also improve the count-rate capability. The authors developed CdTe semiconductor detector-based positron emission tomography (CdTe-PET) and single-photon emission computed tomography (CdTe-SPECT) in order to test the potential of using semiconductor detectors in nuclear medicine. The physical performances of both systems were measured in several phantom experiments. The capability of using CdTe-PET

---

W. Takeuchi (✉) • A. Suzuki • K. Kobashi
Research and Development Group, Hitachi Ltd., 1-280, Higashi-Koigakubo Kokubunji-shi,
Tokyo 185-8601, Japan
e-mail: wataru.takeuchi.rg@hitachi.com

Y. Ueno
Research and Development Group, Hitachi Ltd., 1-280, Higashi-Koigakubo Kokubunji-shi,
Tokyo 185-8601, Japan

Faculty of Engineering, Hokkaido University, Sapporo, Japan

T. Shiga • N. Tamaki
Department of Nuclear Medicine, Graduate School of Medicine, Hokkaido University,
Sapporo, Japan

K. Hirata • S. Okamoto • S. Zhao • K. Kobayashi • S. Watanabe
Graduate School of Medicine, Hokkaido University, Sapporo, Japan

Y. Kuge
Central Institute of Isotope Science, Hokkaido University Department of Integrated Molecular
Imaging, Graduate School of Medicine, Hokkaido University, Sapporo, Japan

N. Kubo
Office of Health and Safety, Hokkaido University, Sapporo, Hokkaido, Japan

K. Umegaki
Faculty of Engineering, Hokkaido University, Sapporo, Japan

Y. Kuge et al. (eds.), *Perspectives on Nuclear Medicine for Molecular Diagnosis and Integrated Therapy*, DOI 10.1007/978-4-431-55894-1_4

to measure the metabolic distribution of tumors was evaluated through scans of cancer patients and rat tumor models. The feasibility of using CdTe-SPECT for simultaneous dual-radionuclide imaging was evaluated through scans of phantoms and healthy volunteers. The results suggest that the prototype CdTe-PET can identify intratumoral metabolic heterogeneous distribution and that CdTe-SPECT can accurately acquire dual-radionuclide images simultaneously. Although there are still problems to be solved, semiconductor detectors will play significant roles in the future of nuclear medicine.

**Keywords** Semiconductor detector • Solid-state detector • CdTe • Intratumoral heterogeneity • Dual radionuclide

## 4.1 Introduction

Nuclear medicine plays a significant role in diagnosis, treatment planning, and treatment response evaluation. In particular, in oncology, biological imaging by positron emission tomography (PET) permits not only tumor detection but also gross tumor delineation and identification of biological heterogeneities [1, 2]. In the delineation of tumor boundaries by PET, achieving a good spatial resolution and quantitative accuracy are physical imaging concerns. The spatial resolution of the current PET images as used in clinical practice is 7–9 mm after reconstruction with many systems. The achievable spatial resolution depends primarily on the size of the detector elements. The typical PET scanner used in current clinical study is comprised of scintillation detectors 4 × 4 mm in size.

In nuclear cardiology and brain nuclear medicine, functional imaging by PET and single-photon emission computed tomography (SPECT) can measure the functional state of the myocardium and brain. Unlike PET, SPECT has the potential to enable simultaneous multi-radionuclide imaging. The scanning of multi-radionuclide pharmaceuticals will enable various kinds of functional images to be obtained without position error or time difference. The recent development of several cardiac SPECT systems that use solid-state detectors with a fine energy resolution [3–5] has led to simultaneous multi-radionuclide imaging recapturing the spotlight. A number of simultaneous multi-radionuclide imaging studies have been reported, especially for myocardial perfusion diagnosis [4, 5]. To enable accurate simultaneous multi-radionuclide imaging, a detector with a good energy resolution is necessary. In addition, improving the sensitivity of gamma-ray detection is also important for realizing simultaneous multi-radionuclide imaging with an appropriate dose of radiopharmaceuticals.

As mentioned above, the performance of nuclear medicine imaging depends on spatial resolution, energy resolution, and sensitivity. Semiconductor detectors, e.g., CdZnTe or CdTe detectors, provide improved energy resolution due to the direct conversion of gamma rays to charge carriers. This fine resolution leads to a better image contrast due to better scatter rejection. Semiconductor detectors also easily provide a pixelated structure that improves the count-rate capability and intrinsic spatial resolution. Flexibility in both sizing and a fine arrangement of semiconductor detectors is expected not only to improve the spatial resolution but also to obtain depth-of-interaction (DOI) information in PET and pixel-of-interaction in SPECT when the multidetector pixels are placed within each collimator hole. A high energy resolution is expected to reduce scattered components in detected signals and to improve the quantitative accuracy of the reconstructed images. These features of semiconductor detectors may lead to improved PET and SPECT images. The authors previously developed CdTe semiconductor detector-based PET (CdTe-PET) [1, 2] and SPECT (CdTe-SPECT) [6, 7]. The physical and clinical performances of the systems were evaluated through phantom, animal, and clinical studies.

## 4.2 Materials and Methods

### *4.2.1 Development and Performance Evaluation of Prototype CdTe-PET*

#### 4.2.1.1 Outline of CdTe-PET and Its Parameter Settings

CdTe-PET is a prototype semiconductor PET scanner for human brain imaging. This scanner is described in detail in a previous report [1]. In brief, the scanner uses CdTe detectors for dedicated three-dimensional emission scanning. It has a patient port with a diameter of 350 mm, a transaxial FOV of 310 mm, and an axial FOV of 250 mm. The size of a detector is $1.0 \times 4.0 \times 7.5$ mm. The detector channel is composed of two CdTe elements in the radial direction and two CdTe elements in the tangential direction. To utilize the depth-of-interaction (DOI) technique, three detector channels (six detectors) in the tangential direction are used. The transverse and axial spatial resolutions near the center are 2.3 and 5.1 mm, respectively. The energy resolution is 4.1 % at 511 keV (FWHM), which is superior to that of available scintillation detectors, e.g., 10–20 %. The long-term stability of the energy resolution of the CdTe detectors was assured by periodically resetting the bias [8]. No significant variances in the spectral peak position and energy resolution of the CdTe detectors were observed for over a year [9].

The energy of detected gamma rays is recorded in list-mode data. This data contains the energy information of two gamma rays in the coincidence detection. The size of an energy bin is 4 keV. Two energy windows, described below, were used. One energy window (390–540 keV) was used as a wide energy window (WEW), and another (494–540 keV) was used as a photopeak energy window (PEW). Sinogram data using both WEW and PEW were made by sorting the list-mode data by recorded energy. For all measured sinogram data and energy spectra, random coincidences were removed by using the delayed coincidence subtraction technique. The size of the sinogram data is 256 in the radial direction, 256 in the angular direction, 87 in the axial direction, and 44 in the oblique angular direction, i.e., ring difference. The matrix size of the reconstructed images is $256 \times 256 \times 87$ with voxels of $1.21 \times 1.21 \times 2.8$ mm.

To bring out the potential of CdTe detectors in human imaging, the main challenge to be solved is sensitivity. The effective atomic number of the CdTe is smaller than the scintillation detectors of the current PET scanner. The crystal size is also smaller than those detectors. To overcome the sensitivity problem, the following improvements were made.

To improve sensitivity, a novel signal processing method was developed [1]. The effective atomic number of the CdTe is 50, so the whole absorption rate of the 511-keV gamma ray is smaller than the current scintillation detectors, and a considerable amount of scattered gamma rays are generated and absorbed in nearby detectors. In the improved signal processing method, when the sum of the energy of two gamma rays detected in a neighborhood channel in a limited time window (64 ns) is around 511 keV, the record of the gamma rays detected at the opposing detector unit in the coincidence time window (14 ns) is checked for the coincidence detection. With this signal processing, the detector of our system is considered to be a continuous mass of CdTe from the viewpoint of sensitivity, although the position is determined digitally.

#### 4.2.1.2 Image Reconstruction Method

A reconstruction system of the developed scanner coped with the sensitivity problem, avoiding unexpected statistical fluctuation in reconstructed images. To enable high-resolution imaging with a low amount of statistical data, we developed a reconstruction method that could suppress statistical noise without degrading the spatial resolution [1, 10]. The method is based on maximum a posteriori (MAP) [11] with median root prior (MRP) [12] and uses a resolution recovery technique [13, 14]. The method also uses an attenuation and normalization weighting technique. MRP assumes only local monotony and does not need any anatomical information such as MRI or CT images. MRP is also known as an effectual prior for reducing noise and preserving edge. Because of various incident angles and distances to detectors, reconstructed point source images blur into various shapes. To correct the point spread function (PSF), a 3-D image-space convolution technique was used [13]. The Gaussian kernel represents the PSF. The algorithm of the reconstruction method, named "point spread function correction with median root prior" (PSC-MRP), is shown in Eq. (4.1):

$$\lambda_j^{k+1} = \frac{\lambda_j^k}{\left(1+\beta\frac{\lambda_j^k - M_j}{M_j}\right)\cdot\left(\sum_i p_{ij}a_j n_j\right)\otimes G}\left(\sum_i p_{ij}\frac{y_i}{\sum_{j'} p_{ij'}\left(\lambda_{j'}^k\otimes G\right)}\right)\otimes G \quad (4.1)$$

$$, \text{where } \begin{array}{l} \lambda : \text{pixelvalue}\ (j = \text{index}, k = \text{iteration}) \\ y : \text{obsereved data}\ (i = \text{index}) \\ p : \text{probability-matrix} \\ a : \text{attenuation-matrix} \\ n : \text{normatlization-matrix} \\ M : \text{median of the neibourhodd} \\ G : \text{Gaussian-Kernel}\ (PSF) \\ \beta : \text{prior strength} \end{array} .$$

The value $y$ is measured data, and λ is emission image. The matrices $p$, $a$, and $n$ represent probability (geometrical sensitivity), attenuation, and normalization (sensitivity of each detector), respectively. The value $k$ is the number of iterations, and $i$ and $j$ are index numbers. The value β controls the effect of reducing noise, and M is a median of neighbor (3 × 3 × 3) voxels' values. The Gaussian kernel $G$ represents the PSF. The PSFs were measured for a point source at different positions in a portion of the field of view. The $G$ was parameterized to correct for point source location and to smooth for projection noise. When β is zero and $G$ is not used, the reconstruction method equals attenuation and normalization weighted OSEM (ANW-OSEM) [15]. The numbers of subsets and iterations were 8 and 5, respectively.

#### 4.2.1.3 Physical Performance Measurement

In accordance with the NEMA NU2-1994 standards [16], a count-rate performance experiment was conducted with CdTe-PET. In this evaluation, two energy windows (WEW and PEW described above) were used. The count-rate performance of CdTe-PET was measured with a standard 20-cm-inner-diameter, 20-cm-long phantom filled with water that contained a 3.7-kBq/cm$^3$ F-18 solution. The phantom was placed at the center of the FOV and scanned over ten half-lives. The performance was evaluated in WEW and PEW settings. The noise equivalent count rate (NEC2R) was calculated by NEC2R = T*T/(T + S + 2*R) from the true (T) rate, scattered (S) rate, and random (R) rate. The random rate was multiplied by a factor of two because the random rate was evaluated by acquiring events in a delayed time window. The sensitivity of the scanner was also evaluated using the measurement data of count-rate performance.

#### 4.2.1.4 Image Quality Evaluation

To evaluate the image quality of CdTe-PET with its energy window set to PEW, two kinds of experiments and studies, described below, were conducted.

### Hoffman Phantom

A Hoffman phantom (filled with 9.1 kBq/ml F-18 solution) simulated the human brain was scanned for 10 min so as to equalize the measured count with the clinical situation. The data was reconstructed by (a) ANW-OSEM, (b) ANW-OSEM with post-reconstruction Gaussian filter (4-mm FWHM), and (c) PSC-MAP $\beta = 0.05$. The three images were compared visually.

### Preclinical Evaluation with Rat Tumor Model

To evaluate the feasibility of visualizing intratumoral heterogeneity, a preclinical study using a rat tumor model was conducted. All animal care and experimental procedures were performed with the approval of the Laboratory Animal Care and Use Committee of Hokkaido University. Eight-week-old male Wistar-King-Aptekman/hok (WKAH) rats (Japan SLC, Inc.) were inoculated with a suspension of allogenic rat glioma cells (C6, 2 × 106 cells/0.2 ml) into the left calf muscle to generate glioma rat models. The rats were allowed free access to water and laboratory chow until the day before the experiment. When the tumors were 1–2 cm in diameter, the rats were fasted overnight. Under diethyl ether anesthesia, 200 kBq/g body weight of F-18-fluorodeoxyglucose (FDG) was intravenously injected into each rat. Fifty minutes after the injection of FDG, the rats were anesthetized with pentobarbital (50 mg/kg body weight, intraperitoneally). One hour after the FDG injection, each rat was scanned by CdTe-PET for 1 min. Then, images were reconstructed by PSC-MAP ($\beta = 0.05$). Four hours after the FDG injection, the rats were euthanized under deep pentobarbital anesthesia. The animals were sacrificed, and the whole tumors were quickly excised. Then, the excised tumors were frozen in isopentane/dry ice. The frozen tumor tissues were sectioned into slices for autoradiographic (ARG) imaging. The thickness of the sectioned slices was 0.15 mm. The number of slices was about 19. All of the sectioned slices were exposed to phosphor imaging plates (BAS-SR 2025, Fuji Photo Film Co., Ltd.) together with a set of calibrated standards. The autoradiographic exposure was performed for 12 h to detect the radioactivity of FDG. After the exposure, the imaging plates were scanned with a Fuji Bio-imaging Analyzer BAS-5000, and the units of the images were converted into a unit of Bq/ml by house-made software. All of the sectioned slices were integrated into a 3-D volume by using a slice-by-slice image registration technique. Then, the integrated 3-D ARG and PET images were compared.

### Clinical Evaluation

As was previously reported [1, 2], patients with brain tumor or nasopharyngeal cancer injected FDG (340 MBq ca.) were scanned by CdTe-PET for 30 min. Then, images were reconstructed by PSC-MAP ($\beta = 0.05$). The patient volunteers gave written, informed consent in accordance with the Helsinki II Declaration. The study was approved by the ethics committees of both the Hokkaido University Graduate School of Medicine and Hitachi, Ltd. The capability of using CdTe-PET to measure the metabolic distribution of tumor was evaluated.

## *4.2.2 Development and Performance Evaluation of Prototype CdTe-SPECT*

### 4.2.2.1 Outline of CdTe-SPECT

CdTe-SPECT is a prototype semiconductor SPECT system for human brain imaging. This system is described in detail in previous reports [6, 7]. In brief, CdTe-SPECT includes two detector heads. Each head consists of 192 × 96 detector pixels with a pitch of 1.4 mm, so the field of view of the detector head is 268 × 134 mm (tangential × axial). The size of each detector pixel is 1.2 × 1.4 × 5 mm. The intrinsic energy resolution (FWHM) of the CdTe detector is 6.6 % at 140.5 keV, and the count-rate linearity is maintained at 200 kcps per head and under [9]. For high-sensitivity imaging, a wide aperture parallel-hole collimator (Fig. 4.1), which we call the “4-pixel matched collimator” (4-PMC), was previously developed [6, 7]. The hole size of the 4-PMC is matched to four detector pixels, that is, there are four (2 × 2) pixels per collimator hole. By contrast, the hole size of the standard parallel-hole collimator [9] is matched to one detector pixel, that is, a 1-pixel matched collimator (1-PMC). The specifications of both collimators are shown in Table 4.1. 4-PMC was designed to improve the sensitivity and spatial resolution in clinical SPECT imaging compared with 1-PMC. The sensitivities of 1-PMC and 4-PMC were 70 and 220 cps/MBq/head, respectively [7]. Therefore, 4-PMC has three times the sensitivity of 1-PMC. The rotation radius of the detector head is set to 130 mm for brain scans. In SPECT acquisition, each detector head is rotated by 360° over 3 min.

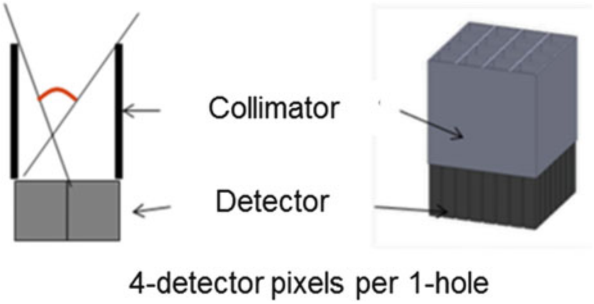

**Fig. 4.1** Geometry of 4-PMC

**Table 4.1** Collimator specifications

| Type | Hole pitch (mm) | Hole size (mm) | Hole length (mm) | Sensitivity (cps/MBq/head) |
|---|---|---|---|---|
| 1-PMC | 1.4 | 1.12 | 20.0 | 70 |
| 4-PMC | 2.8 | 2.40 | 26.0 | 220 |

#### 4.2.2.2 Image Reconstruction Method

The ordered subset expectation maximization (OSEM) (Hudson and Larkin 1994) including PSF and attenuation correction was used. The PSF of each collimator type was obtained by ray-tracing simulation [6, 7]. The attenuation factor of the gamma rays in a subject was approximated by an exponential function of the line integral from an image pixel to a detector pixel in an attenuation map. The projection image matrix size (tangential × axial) was 256 × 96 (pixel size = 1.4 × 1.4 mm). The number of projection images was 120 over 360°. The reconstructed image matrix size (x × y × z) was 256 × 256 × 96 (pixel size = 1.4 × 1.4 × 1.4 mm). The numbers of subsets and iterations were 30 and 20, respectively. The reconstructed images were smoothed with a 14-mm FWHM Gaussian filter.

#### 4.2.2.3 Performance Evaluation in Phantom Experiment and Clinical Study

##### Dual-Radionuclide Character-Shape Phantom

A character-shape dual-radionuclide phantom, which has three kinds of radioactivity, was scanned (Fig. 4.2). The activities are shown in Table 4.2. The photopeak energy windows for Tc-99m (141 keV) and I-123(159 keV) were 130–148 keV and 155–170 keV, respectively. An energy window-based scatter correction based on the triple energy window (TEW) method [17] was used. The measured energy spectrum and reconstructed images were evaluated.

##### Simultaneous Dual-Radionuclide Human Brain Study

A healthy volunteer was injected with Tc-99m HAS-D and I-123 IMP and then scanned by CdTe-SPECT for 21 min as a simultaneous dual-radionuclide brain study. The healthy volunteer gave written, informed consent in accordance with the Helsinki II Declaration. The study was approved by the ethics committees of both the Hokkaido University Graduate School of Medicine and Hitachi, Ltd. The

**Fig. 4.2** Dual-radionuclide character-shape phantom

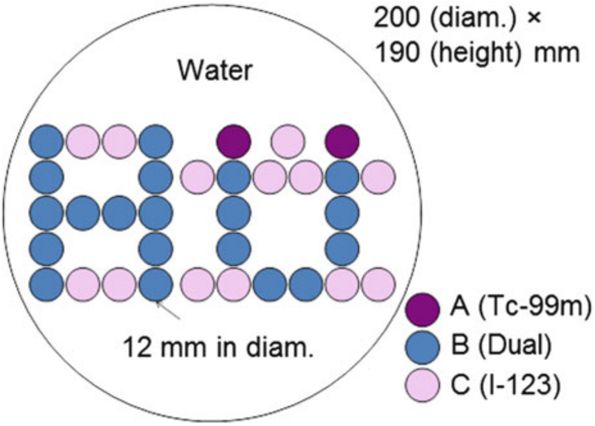

**Table 4.2** Radioactivities of dual-radionuclide character-shape phantom

| Kinds of vial | Tc-99m (kBq/ml) | I-123 (kBq/ml) |
|---|---|---|
| A (Tc-99m) | 44.6 | 0 |
| B (Dual) | 49.3 | 115.5 |
| C (I-123) | 0 | 101 |

feasibility of using CdTe-SPECT for simultaneous dual-radionuclide study was evaluated.

## 4.3 Results and Discussion

### 4.3.1 Performance Evaluation of CdTe-PET by Phantom Experiment and Clinical Study

#### 4.3.1.1 Physical Performance of CdTe-PET

Figure 4.3 shows the result of the count-rate performance examination. The left vertical axis is the count rate of “true” and “random.” The right vertical axis is the noise equivalent count rate (NEC2R). The horizontal axis is the activity of the cylinder phantom. Table 4.3 shows the results for sensitivity, NECR, and scatter fraction. The sensitivity was 22.0 and 8.5 kcps/(kBq/ml) in WEW and PEW, respectively. The NECR at 7.4 kBq/ml was 45 and 25 kcps in WEW and PEW, respectively. The scatter fraction was 39 and 12 % in WEW and PEW, respectively. Comparing PEW with WEW, although the sensitivity was less than a half, the NECR was more than a half. The scatter fraction for PEW was less than a third of that for WEW.

**Fig. 4.3** Count-rate performance

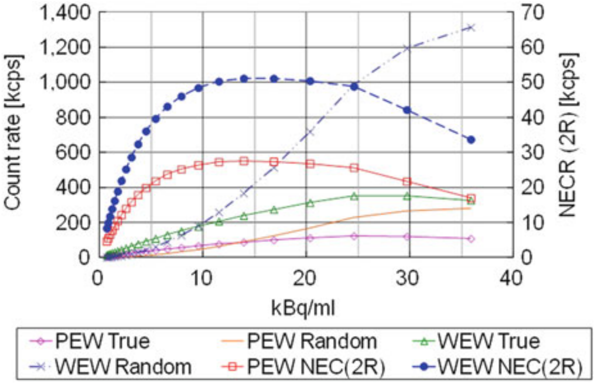

**Table 4.3** Count-rate performances in each energy window

| Energy window | WEW | PEW |
|---|---|---|
| Sensitivity [kcps/(kBq/ml)] | 22.0 | 8.5 |
| Peak NECR [kcps] | 51 | 28 |
| NECR at 3.7 kBq/ml [kcps] | 32 | 18 |
| NECR at 7.4 kBq/ml [kcps] | 45 | 25 |
| Scatter fraction [%] | 39 | 12 |

#### 4.3.1.2 Image Quality of CdTe-PET

Hoffman Phantom

Shown in Fig. 4.4 are images reconstructed by (a) ANW-OSEM, (b) ANW-OSEM with a Gaussian filter (4-mm FWHM), and (c) PSC-MAP $\beta = 0.05$. Even with filtering, images reconstructed by ANW-OSEM had speckle noise. The PSC-MAP image was not speckled and not blurred. Therefore, the edge between gray matter and white matter in the PSC-MAP image was well defined.

Preclinical Evaluation with Rat Tumor Model

The diameter of each tumor was ca. 16 mm. A 3-D ARG volume made by integrating 19 slices is shown in Fig. 4.5. The heterogeneous intratumoral FDG distribution in each tumor was visualized by both CdTe-PET and ARG (Figs. 4.5 and 4.6). CdTe-PET images were visually consistent with ARG (Fig. 4.6).

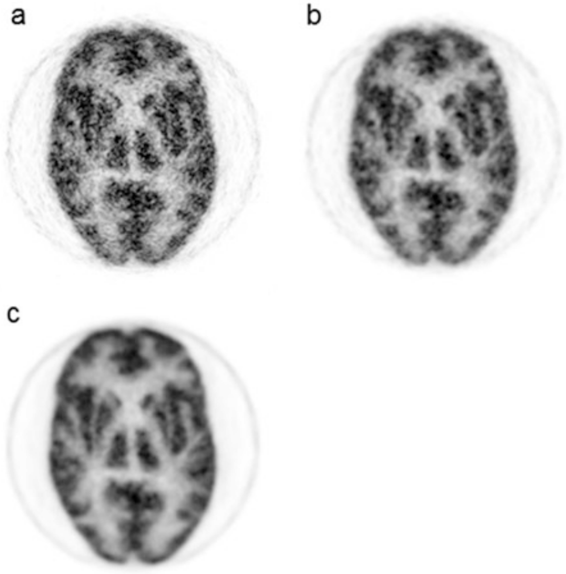

**Fig. 4.4** Reconstructed image of Hoffman phantom. (**a**) ANW-OSEM, (**b**) ANW-OSEM + Gaussian filter, and (**c**) PSC-MAP (b = 0.05)

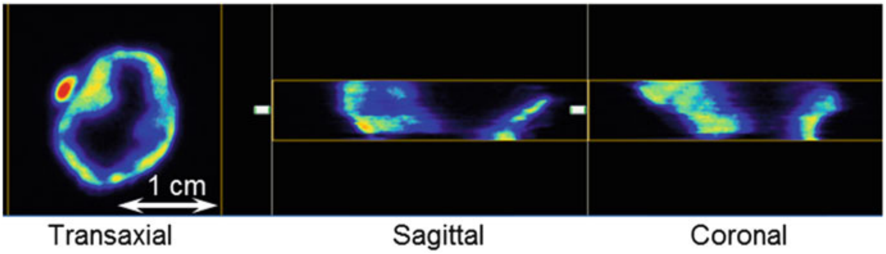

**Fig. 4.5** Integrated 3-D ARG volume

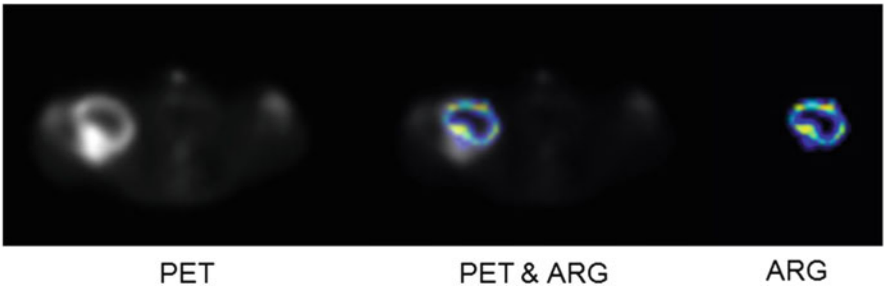

**Fig. 4.6** Comparison of ARG and PET images. “PET + ARG” shows image fused by image registration method

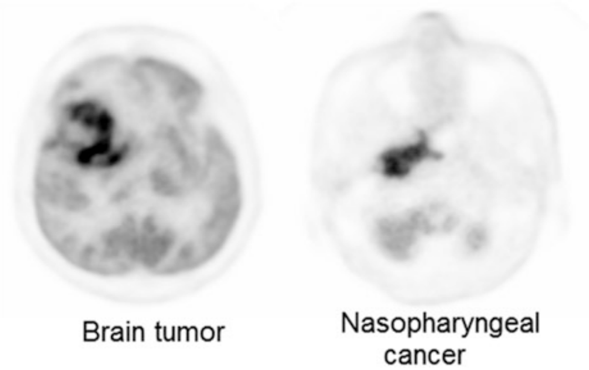

**Fig. 4.7** Clinical image example of brain tumor patient and nasopharyngeal cancer patient

Clinical Evaluation

Reconstructed images of brain tumor and nasopharyngeal cancer patients scanned by CdTe-PET are shown in Fig. 4.7. CdTe-PET identified intratumoral heterogeneity and visualized the tumor's edge sharply for both cancers.

## *4.3.2 Performance Evaluation of CdTe-SPECT by Phantom Experiment and Clinical Study*

### 4.3.2.1 Dual-Radionuclide Character-Shape Phantom

The photopeaks of Tc-99m and I-123 were clearly discriminated in the measured energy spectrum (Fig. 4.8). The energy resolution of the CdTe semiconductor detector was high enough to separate the photopeaks of Tc-99m and I-123. The scatter-corrected images of Tc-99m and I-123 were clearly discriminated in the character-shape phantom image in Fig. 4.9. Because of the high-energy resolution of the CdTe semiconductor detector, there was no Tc-99m contamination in the I-123 window image even without scatter correction. The results suggested that simultaneous Tc-99m and I-123 study by using CdTe-SPECT was feasible.

### 4.3.2.2 Simultaneous Dual-Radionuclide Human Brain Study

The result of a simultaneous Tc-99m and I-123 dual-radionuclide scan is shown in Fig. 4.10. The Tc-99m HSAD and I-123 IMP images were clearly discriminated. The result suggests that CdTe-SPECT has the potential to produce accurate brain

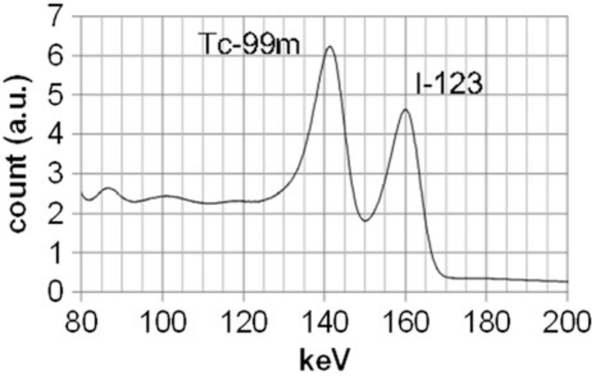

**Fig. 4.8** Energy spectrum of dual-radionuclide character-shape phantom measurement

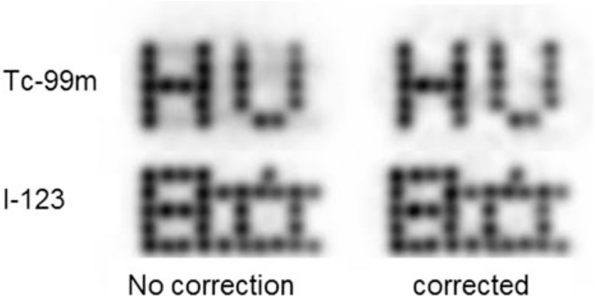

**Fig. 4.9** Reconstructed image of dual-radionuclide character-shape phantom

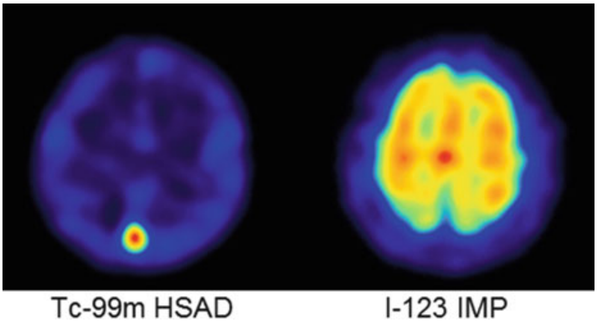

**Fig. 4.10** Reconstructed image of simultaneous dual-radionuclide brain study

perfusion images (Tc-99m HSAD) and cerebral blood volume (Tc-99m HSAD) images simultaneously.

## 4.4 Conclusion

Prototype CdTe-PET and CdTe-SPECT systems were developed, and their performances were evaluated. The results suggest that CdTe-PET enables better identification of intratumoral metabolic distribution and that CdTe-SPECT will enable simultaneous dual-radionuclide brain study to become available clinically. Semiconductor detectors have the potential to play a significant role in the future of nuclear medicine.

**Acknowledgments** This work was supported in part by the Creation of Innovation Centers for Advanced Interdisciplinary Research Areas Program, Ministry of Education, Culture, Sports, Science and Technology, Japan.

## References

1. Morimoto Y, Ueno Y, Takeuchi W, Kojima S, Matsuzaki K, Ishitsu T, et al. Development of a 3D brain PET scanner using CdTe semiconductor detectors and its first clinical application. IEEE Trans Nucl Sci. 2011;58:2181–9.
2. Shiga T, Morimoto Y, Kubo N, Katoh C, Takeuchi W, Usui R, et al. A new PET scanner with semiconductor detectors enables better identification of intratumoral inhomogeneity. J Nucl Med. 2009;50:148–55.
3. Kubo N, Zhao S, Fujiki Y, Kinda A, Motomura N, Katoh C, et al. Evaluating performance of a pixel array semiconductor SPECT system for small animal imaging. Ann Nucl Med. 2005;19:633–9.
4. Bocher M, Blevis IM, Tsukerman L, Shrem Y, Kovalski G, Volokh L. A fast cardiac gamma camera with dynamic SPECT capabilities: design, system validation and future potential. Eur J Nucl Med Mol Imaging. 2010;37:1887–902.
5. Ko T, Utanohara Y, Suzuki Y, Kurihara M, Iguchi N, Umemura J, et al. A preliminary feasibility study of simultaneous dual-isotope imaging with a solid-state dedicated cardiac camera for evaluating myocardial perfusion and fatty acid metabolism. Heart Vessel. 2014. doi:10.1007/s00380-014-0578-4.
6. Suzuki A, Takeuchi W, Ishitsu T, Tsuchiya K, Ueno Y, Kobashi K. A four-pixel matched collimator for high-sensitivity SPECT imaging. Phys Med Biol. 2013;58:2199–217.
7. Suzuki A, Takeuchi W, Ishitsu T, Tsuchiya K, Morimoto Y, Ueno Y, et al. High-sensitivity brain SPECT system using cadmium telluride (CdTe) solid-state detector and 4-pixel matched collimator. Phys Med Biol. 2013;58:7715–31.
8. Seino T, Kominami S, Ueno Y, Amemiya K. Pulsed bias voltage shutdown to suppress the polarization effect for a CdTe radiation detector. IEEE Trans Nucl Sci. 2008;55:2770–4.
9. Tsuchiya K, Takahashi I, Kawaguchi T, Yokoi K, Morimoto Y, Ishitsu T, et al. Basic performance and stability of a CdTe solid-state detector panel. Ann Nucl Med. 2010;24:301–11.
10. Takeuchi W, Morimoto Y, Suzuki A, Matsuzaki K, Kojima S, Kobashi K, et al. Iterative reconstruction method using prior information and point spread function for high resolution CdTe PET scanner. J Nucl Med(Meeting abstract). 2008;49:388.

11. Green PJ. Bayesian reconstructions from emission tomography data using a modified EM algorithm. IEEE Trans Med Imaging. 1990;9:84–93.
12. Alenius S, Ruotsalainen U. Generalization of median root prior reconstruction. IEEE Trans Med Imaging. 2002;21:1413–20.
13. Reader AJ, Julyan PJ, Williams H, Hastings DL, Zweit J. EM algorithm system modeling by image-space techniques for PET reconstruction. IEEE Trans Nucl Sci. 2003;50:1392–7.
14. Panin VY, Kehren F, Michel C, Casey M. Fully 3-D PET reconstruction with system matrix derived from point source measurements. IEEE Trans Med Imaging. 2006;25:907–21.
15. Zaidi H. Quantitative analysis in nuclear medicine imaging. New York: Springer; 2006. p. 167–204.
16. NEMA. NEMA standards publication NU2-1994. 1994.
17. Ichihara T, Ogawa K, Motomura N, Kubo A, Hashimoto S. Compton scatter compensation using the triple-energy window method for single- and dual-isotope SPECT. J Nucl Med. 1993;34:2216–21.

# Chapter 5
# Kinetic Analysis for Cardiac PET

**Yuuki Tomiyama and Keiichiro Yoshinaga**

**Abstract** *Objective:* PET has the ability to evaluate functional information as well as visualization of radiotracer uptake. Compartmental model is a basic idea to analyze dynamic PET data. C-HED has been the most frequently used PET tracer for the evaluation of cardiac sympathetic nervous system (SNS) function. The washout of norepinephrine from myocardium is associated with increasing SNS activity in heart failure (HF). However, the existence of washout of $^{11}$C-HED from the myocardium is controversial. Although "retention index" (RI) is commonly calculated to quantify the uptake of HED, RI is not purely able to distinguish washout parameter and uptake parameter. Therefore, in this study, we aimed to evaluate whether HED was washed out from the myocardium using compartment model analysis.

*Material and Methods:* We compared HED parameters in ten normal volunteers (32.4 ± 9.6 years) and nine HF patients (age: 57.3 ± 17.3 years, LVEF: 36.1 ± 16.7 %). Each subject underwent rest $^{11}$C-HED PET. We estimated RI, inflow rate K1, and washout rate k2 using single-compartment model analysis using $^{11}$C-HED PET.

*Result:* HF patients showed lower RI and inflow rate K1 compared to normal volunteers (RI: 0.06 ± 0.02 vs. 0.15 ± 0.03 $\text{min}^{-1}$, $p < 0.001$, K1: 0.14 ± 0.05 vs 0.20 ± 0.03 ml/min/g, $p < 0.001$). Washout rate k2 also significantly increased in HF patients (k2: 0.036 ± 0.026 vs. 0.016 ± 0.011 $\text{min}^{-1}$, $p = 0.041$).

*Conclusion:* HF patients showed reduced RI, reduced K1, and higher washout rate k2 compared to normal. This result may imply that HED PET is able to evaluate washout parameter using compartment model.

**Keywords** Compartment model analysis • $^{11}$C-Hydroxyephedrine • Retention index • Sympathetic nervous system function

---

Y. Tomiyama (✉)
Department of Nuclear Medicine, Hokkaido University Graduate School of Medicine, Kita15 Nishi7, Kita-Ku, Sapporo 060-8638, Hokkaido, Japan
e-mail: tomiyamayuuki@frontier.hokudai.ac.jp

K. Yoshinaga
Department of Nuclear Medicine, Hokkaido University Graduate School of Medicine, Kita15 Nishi7, Kita-Ku, Sapporo 060-8638, Hokkaido, Japan

Molecular Imaging Research Center, National Institute of Radiological Sciences, 4-9-1 Anagawa, Inage-Ku, Chiba 263-8555, Japan

Y. Kuge et al. (eds.), *Perspectives on Nuclear Medicine for Molecular Diagnosis and Integrated Therapy*, DOI 10.1007/978-4-431-55894-1_5

## 5.1 Introduction

Positron emission tomography (PET) is a powerful tool to evaluate functional information imaging as well as anatomical information [1, 2]. PET is the most reliable modality for assessing functional information, especially in cardiovascular imaging [3, 4]. When biomedical functions are analyzed using PET images, compartment model analysis is generally applied [5, 6]. Compartment model analysis enables to observe the pharmacokinetics of radiotracer in human body. Thus, we apply compartment model analysis to evaluating pharmacokinetics of $^{11}$C-hydroxyephedrine (HED).

$^{11}$C- HED has been the most frequently used PET tracer for the estimation of cardiac sympathetic nervous system (SNS) function [7–9]. In general, $^{11}$C- HED data has been evaluated using the retention index (RI) [8]. RI is a parameter that can be calculated easily compared to other quantitative parameters. RI includes uptake and washout parameters. However, RI does not differentiate washout parameters from cardiac HED data. Cardiac washout parameter is widely used for evaluation of SNS function and increased cardiac washout is associated with cardiac events in heart failure (HF) [10]. Therefore, it would be important to evaluate the washout parameters using HED PET. Compartment model analysis might have a potential to evaluate precise pharmacokinetics of $^{11}$C-HED and also has a potential to evaluate purely washout parameter [11].

In this study, we aimed to analyze HED uptake parameter and washout parameter using single-compartment model analysis in patients with HF.

## 5.2 Methods

### 5.2.1 Study Subjects

Ten healthy volunteers and nine HF patients participated in the current study. The healthy volunteers (ten men, 32.4 ± 9.6 years) had a low pretest likelihood of coronary artery disease (<5 %) based on risk factors [12]. HF patients were recruited from a group of patients who underwent HED PET for the assessment of sympathetic neuronal function. They were six men and three women (57.3 ± 17.3 years). The study was approved by the Hokkaido University Graduate School of Medicine Human Research Ethics Board. Written informed consent was obtained from all participants.

### 5.2.2 Positron Emission Tomography/Computed Tomography $^{11}$C-HED PET/CT Imaging

$^{11}$C-HED was produced from $^{11}$C-methyl iodide and metaraminol (free base) using standard methods with high purity and high specific activity [13].

All participants were instructed to fast overnight. PET/CT imaging was performed with a 64-slice PET/CT scanner (Biograph Siemens/CTI, Knoxville, TN, USA). A low-dose CT was performed for attenuation correction. The CT co-registered to standard orthogonal PET images was then re-sliced into series of short-axis, horizontal long-axis, and vertical long-axis images.

Immediately after the administration of 5 mCi(185 MBq) of intravenous $^{11}$C-HED, participants underwent 40-min 3D list-mode PET acquisition. The images were reconstructed using filtered back correction with a12-mm Hann filter and were reconstructed into 23 frames ($10 \times 10$ s; $1 \times 60$ s; $5 \times 100$ s; $3 \times 180$ s; $4 \times 300$ s) [14].

### 5.2.3 RI Estimation

RI is obtained by normalizing late phase of tracer activity concentrations (30–40 min) of left ventricular (LV) myocardium divided by the integral of the arterial input function (AIF). The time-activity curve was derived from a small circular region of interest in the left ventricular cavity (Fig. 5.1, [10]).

### 5.2.4 Compartment Model Analysis

Harms HJ et al. reported the single-tissue model was more robust than two-tissue compartment model and results obtained were similar to more precise models [11]. Thus, we used single-compartment model to evaluate $^{11}$C-HED washout parameter.

In single-compartment model analysis, tracer kinetics are consisted by only two parameters, which are inflow rate K1 and washout rate k2 (Fig. 5.1, [6]). In this study, K1 and k2 were estimated using the nonlinear least squares method. This approach used AIF arterial input function and tissue activity carve (TAC) of LV myocardium [15, 16]. Distribution volume was also calculated [17]. The equation of distribution volume was inflow rate K1 divided by washout rate k2.

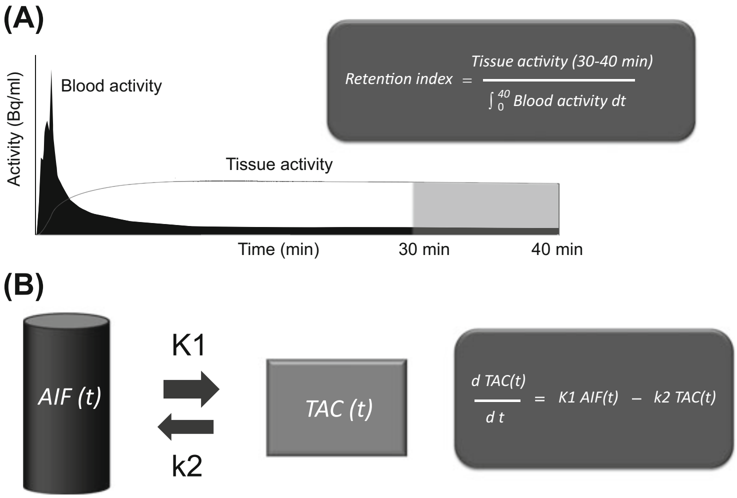

**Fig. 5.1** Analysis methods of $^{11}$C-hydroxyephedrine. (**a**) Calculation method of retention index: retention index was obtained by normalizing late activity concentrations of left ventricular myocardium divided by the integral of the arterial input function.(**b**) Single-tissue compartment model: single-tissue compartment model enables to monitor inflow rate K1 and washout rate k2 of radiotracer between arterial input function (AIF) and tissue activity curve (TAC). AIF and TAC were obtained from LV cavity and myocardial tissue, respectively

### *5.2.5 Statistical Analysis*

Data are expressed as mean ± SD. The differences between the means of two volumetric results were examined using the unpaired two *t*-test. Fisher's exact tests were used for categorical variables. *P*-value of less than 0.05 was considered indicative of a statistically significant difference. Statistical calculations were carried out using JMP software version 12.0 (SAS Institute, Inc., Cary, NC).

## 5.3 Results

### *5.3.1 Subjects' Background*

Table 5.1 summarizes the baseline characteristics of the volunteers and HF patients. HF patients also had laboratory data and echocardiography data. The HF patients were older than normal.

**Table 5.1** The baseline characteristics

| | Normal volunteers ($n = 10$) | Heart failure patients ($n = 9$) | $P$-value |
|---|---|---|---|
| Age (year) | 32.4 ± 9.6 | 57.3 ± 17.3 | <0.001 |
| Sex (M/F) | 10/0 | 6/3 | 0.09 |
| Height (cm) | 172.7 ± 8.8 | 162.2 ± 8.4 | <0.001 |
| Wight (kg) | 68.2 ± 13.5 | 56.8 ± 17.4 | <0.001 |
| Laboratory data | | | |
| BNP (pg/ml) | – | 633.7 ± 876.8 | – |
| Plasma noradrenalin (pg/ml) | – | 469.4 ± 317.7 | – |
| Urinary noradrenaline (μg/day) | – | 127.9 ± 54.5 | – |
| Echocardiography | | | |
| LVEF (%) | – | 36.1 ± 16.7 | – |
| LVEDV (ml) | – | 180.2 ± 95.2 | – |

Data expressed as mean ± SD. *BNP* brain natriuretic peptide, *LVEF* left ventricular ejection fraction, *LVEDV* left ventricular end-diastolic volume, *M* male, *F* female

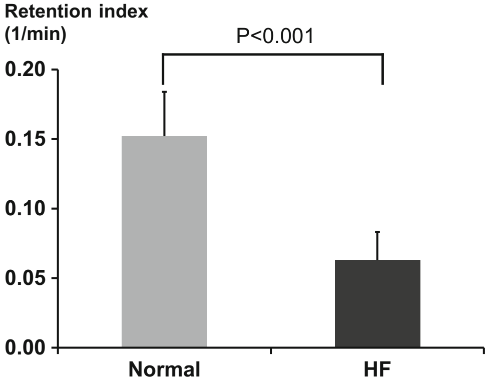

**Fig. 5.2** Difference of retention index between the heart failure and normal. Heart failure patients showed significantly decreased RI compared to normal volunteers

### 5.3.2 *HED PET Data Normal Volunteers and HF Patients*

HF patients significantly decreased RI compared to normal volunteers (0.060 ± 0.020 vs. 0.150 ± 0.032 1/min, $P < 0.001$, Fig. 5.2). In compartment model analysis, HF patients showed decreased inflow rate K1 (0.14 ± 0.03 vs. 0.20 ± 0.05 ml/min/g, $P = 0.004$, Fig. 5.3a) and reduced distribution volume (5.17 ± 2.93 vs. 22.4 ± 23.1 mL/g, $P = 0.04$, Fig. 5.3c). In addition, HF patients significantly increased washout rate k2 compared to normal volunteers (0.036 ± 0.026 vs. 0.016 ± 0.011 1/min, $P = 0.044$, Figs. 5.3b and 5.4.).

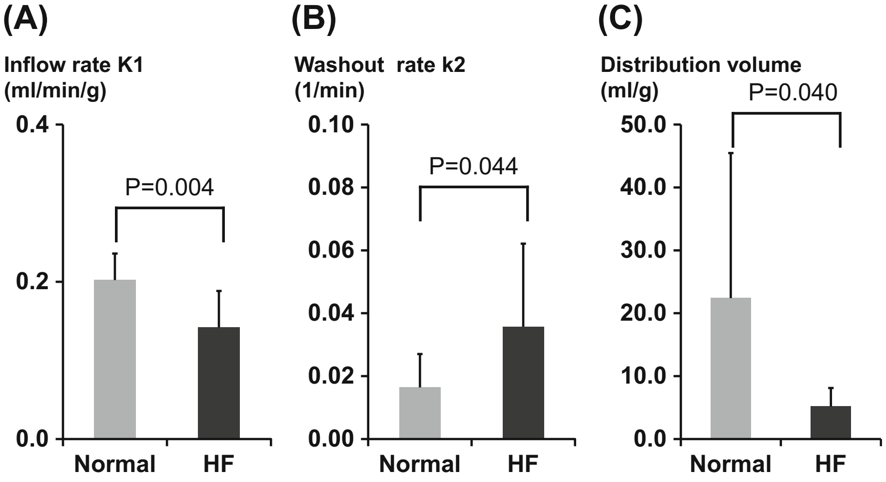

**Fig. 5.3** Difference of parameters calculated using compartment model analysis. Heart failure patients showed significantly decreased inflow rate K1 and distribution volume (**a**, **c**). Heart failure patients also showed significantly decreased washout rate k1 (**b**)

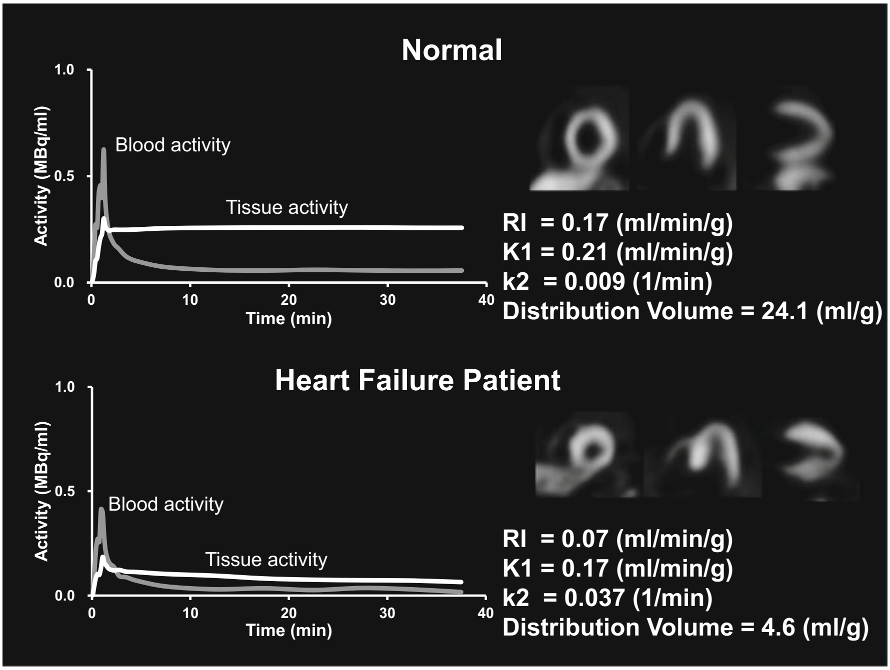

**Fig. 5.4** Example of myocardial time activity curveswith$^{11}$C-hydroxyephedrine. Heart failure patient's time-activity curve showed enhanced washout compared to normal volunteer's one

## 5.4 Discussion

HF patients showed decreased RI, inflow rate K1, and distribution volume compared to normal volunteers. In contrast, the HF patients increased washout parameter k2.

Many previous studies reported patients with imparted SNS function showed lower $^{11}$C-HED uptake [8, 17]. Thus, the present data agree with previous reports.

In this study, HF patients showed significantly increased washout rate k2 compared to normal volunteers. Previous studies using $^{123}$I-MIBG reported HF patient showed increased washout rate [10, 18]. Previous study also reported that washout parameter of $^{11}$C-HED was well correlated with plasma and cardiac norepinephrine in experiments with rats [7]. Therefore, current data that HF patient showed increased washout rate may be considered to be appropriate.

### *5.4.1 Study Limitation*

Our study had a small population and HF patients were significantly older than normal volunteers. Therefore, further investigations with larger and age-matched populations are required.

In addition, washout parameters were not compared to other clinical indexes. Comparison washout of $^{11}$C-HED and other clinical parameter such as ejection fraction, laboratory parameter, and washout of $^{123}$I-MIBG should be the next step.

## 5.5 Conclusion

In this study, we applied compartment model analysis to evaluating washout of $^{11}$C-hydroxyephedrine (HED).

As a result, HF patients showed reduced RI, K1, and distribution volume and higher washout rate k2 compared to normal. This result may imply that HED PET is able to evaluate washout parameter using compartment model.

**Conflicts of Interest** None

**Acknowledgments** The authors thank Keiichi Magota, PhD; Ken-ichi Nishijima, PhD; Daisuke Abo, MSc; and Eriko Suzuki for their support for this study. This manuscript has been reviewed by a North American English-language professional editor Ms. Holly Beanlands. The authors also thank Ms. Holly Beanlands for critical reading of the manuscript.

This study was supported in part by grants from the Japanese Ministry of Education, Culture, Sports, Science and Technology (Category B, No. 23390294) and grants from the Innovation Program of the Japan Science and Technology Agency. Tomiyama was supported by postgraduate students' Travel Award Program by Hokkaido University. Dr. Yoshinaga is supported by the Imura Clinical Research Award (Adult Vascular Disease Research Foundation).

## References

1. Yoshinaga K, Burwash IG, Leech JA, Haddad H, Johnson CB, deKemp RA, Garrard L, Chen L, Williams K, DaSilva JN, Beanlands RS. The effects of continuous positive airway pressure on myocardial energetics in patients with heart failure and obstructive sleep apnea. J Am Coll Cardiol. 2007;49:450–8.
2. Katoh C, Morita K, Shiga T, Kubo N, Nakada K, Tamaki N. Improvement of algorithm for quantification of regional myocardial blood flow using 15O-water with PET. J Nucl Med. 2004;45:1908–16.
3. Tomiyama Y, Manabe O, Oyama-Manabe N, Naya M, Sugimori H, Hirata K, Mori Y, Tsutsui H, Kudo K, Tamaki N, Katoh C. Quantification of myocardial blood flow with dynamic perfusion 3.0 Tesla MRI: validation with o-water PET. J Magn Reson Imaging. 2015;42(3):754–62.
4. Kikuchi Y, Oyama-Manabe N, Naya M, Manabe O, Tomiyama Y, Sasaki T, Katoh C, Kudo K, Tamaki N, Shirato H. Quantification of myocardial blood flow using dynamic 320-row multi-detector CT as compared with (1)(5)O-H(2)O PET. Eur Radiol. 2014;24:1547–56.
5. Yoshinaga K, Tomiyama Y, Suzuki E, Tamaki N. Myocardial blood flow quantification using positron-emission tomography: analysis and practice in the clinical setting. Circ J. 2013;77:1662–71.
6. Klein R, Beanlands RS, deKemp RA. Quantification of myocardial blood flow and flow reserve: technical aspects. J Nucl Cardiol. 2010;17:555–70.
7. Thackeray JT, Renaud JM, Kordos M, Klein R, Dekemp RA, Beanlands RS, DaSilva JN. Test-retest repeatability of quantitative cardiac 11C-meta-hydroxyephedrine measurements in rats by small animal positron emission tomography. Nucl Med Biol. 2013;40:676–81.
8. Schwaiger M, Kalff V, Rosenspire K, Haka MS, Molina E, Hutchins GD, Deeb M, Wolfe Jr E, Wieland DM. Noninvasive evaluation of sympathetic nervous system in human heart by positron emission tomography. Circulation. 1990;82:457–64.
9. Bengel FM, Ueberfuhr P, Ziegler SI, Nekolla S, Reichart B, Schwaiger M. Serial assessment of sympathetic reinnervation after orthotopic heart transplantation. A longitudinal study using PET and C-11 hydroxyephedrine. Circulation. 1999;99:1866–71.
10. Matsunari I, Aoki H, Nomura Y, Takeda N, Chen WP, Taki J, Nakajima K, Nekolla SG, Kinuya S, Kajinami K. Iodine-123 metaiodobenzylguanidine imaging and carbon-11 hydroxyephedrine positron emission tomography compared in patients with left ventricular dysfunction. Circ Cardiovasc Imaging. 2010;3:595–603.
11. Harms HJ, de Haan S, Knaapen P, Allaart CP, Rijnierse MT, Schuit RC, Windhorst AD, Lammertsma AA, Huisman MC, Lubberink M. Quantification of [(11)C]-meta-hydroxyephedrine uptake in human myocardium. EJNMMI Res. 2014;4:52.

12. Diamond GA, Forrester JS. Analysis of probability as an aid in the clinical diagnosis of coronary-artery disease. N Engl J Med. 1979;300:1350–8.
13. Rosenspire KC, Haka MS, Van Dort ME, Jewett DM, Gildersleeve DL, Schwaiger M, Wieland DM. Synthesis and preliminary evaluation of carbon-11-meta-hydroxyephedrine: a false transmitter agent for heart neuronal imaging. J Nucl Med. 1990;31:1328–34.
14. Allman KC, Wieland DM, Muzik O, Degrado TR, Wolfe Jr ER, Schwaiger M. Carbon-11 hydroxyephedrine with positron emission tomography for serial assessment of cardiac adrenergic neuronal function after acute myocardial infarction in humans. J Am Coll Cardiol. 1993;22:368–75.
15. Katoh C, Yoshinaga K, Klein R, Kasai K, Tomiyama Y, Manabe O, Naya M, Sakakibara M, Tsutsui H, deKemp RA, Tamaki N. Quantification of regional myocardial blood flow estimation with three-dimensional dynamic rubidium-82 PET and modified spillover correction model. J Nucl Cardiol. 2012;19:763–74.
16. Mori Y, Manabe O, Naya M, Tomiyama Y, Yoshinaga K, Magota K, Oyama-Manabe N, Hirata K, Tsutsui H, Tamaki N, Katoh C. Improved spillover correction model to quantify myocardial blood flow by 11C-acetate PET: comparison with 15O-H 2O PET. Ann Nucl Med. 2015;29:15–20.
17. Schafers M, Dutka D, Rhodes CG, Lammertsma AA, Hermansen F, Schober O, Camici PG. Myocardial presynaptic and postsynaptic autonomic dysfunction in hypertrophic cardiomyopathy. Circ Res. 1998;82:57–62.
18. Boogers MJ, Borleffs CJ, Henneman MM, van Bommel RJ, van Ramshorst J, Boersma E, Dibbets-Schneider P, Stokkel MP, van der Wall EE, Schalij MJ, Bax JJ. Cardiac sympathetic denervation assessed with 123-iodine metaiodobenzylguanidine imaging predicts ventricular arrhythmias in implantable cardioverter-defibrillator patients. J Am Coll Cardiol. 2010;55:2769–77.